Emplacement of multiple magma sheets and wall rock deformation: Trachyte Mesa intrusion, Henry Mountains, Utah

Sven Morgan [a,*], Amy Stanik [a], Eric Horsman [b], Basil Tikoff [b], Michel de Saint Blanquat [c], Guillaume Habert [c]

[a] *Department of Geology, Central Michigan University, Brooks Hall, Mt. Pleasant, MI 48859, USA*
[b] *Department of Geology and Geophysics, University of Wisconsin, Madison, WI 53706, USA*
[c] *UMR 5563/LMTG, Observatoire Midi-Pyrénées, CNRS/Université Paul-Sabatier, 38 rue des 36-Ponts, 31400 Toulouse, France*

Abstract

A detailed structural and rock magnetic study of the Trachyte Mesa intrusion and deformed sedimentary wall rocks, Henry Mountains, Utah, indicates that the intrusion grew vertically and horizontally by the accumulation of multiple horizontal magma sheets. 2−3 cm thick shear zones recognized by intensely cataclasized plagioclase phenocrysts define the contact between sheets. Sheets have bulbous and / or steep frontal terminations and are flat on top. The foliation within the interior of the sheets, near the frontal termination, is subvertical. This steep foliation rotates into the subhorizontal shear zones near the top and bottom contacts and provides a magma flow direction indicator. Away from the frontal termination, the interior foliation rotates to become subhorizontal, similar to the fabric in recent analog experimental studies. Sheets are interpreted as being emplaced as plug flows. Both the field fabric and the rock magnetic data collected from 103 locations on the top of the intrusion and from 73 locations along a vertical cross section exposed in a stream gorge support a multi-stage model of intrusion growth. Emplacement begins as narrow magma channels and magma spreads radially outward from the channels to form sheets. Sheets are stacked upon one another and stop at the same lateral termination. The deformation of the sandstones at the margin of the intrusion, which are rotated upward from the margin to become the roof, is partitioned into layer parallel extension, shearing and layer-parallel shortening components. Bulk strain within the thickest sandstone layer indicates ∼20% thinning and microstructures indicate that the thinning was accommodated by grain-scale fracture-induced porosity collapse. Extension occurred as the layer was stretched over the margin of the rising intrusion. Shearing and layer-parallel shortening are a result of coupling with the underlying sheets as they advanced and accommodated through numerous faults parallel to bedding and at low angles to bedding. The deformation of thinner sedimentary layers is consistent with the sedimentary layering immediately in front of an advancing sheet being translated upward and over the top of the sheet as the hinge zone migrates with the front edge of the advancing sheet.
© 2008 Elsevier Ltd. All rights reserved.

Keywords: Laccolith; Magma sheets; Plug flow; Strain analysis

1. Introduction

In the last ten years evidence has been accumulating that many intrusions were emplaced incrementally from small batches of magma. As a result, the concept of plutons as large crustal magma chambers is being reassessed. For example, using field relationships and AMS data, McNulty et al. (1996) and Mahan et al. (2003) interpreted the emplacement of elongate plutons in the central Sierra Nevada of California as an accumulation of dikes. Elliptical plutons are even interpreted to be a result of several phases of magma inflation (Johnson and Vernon, 2004). Geochronologic data from some classic intrusive suites also support this interpretation. The intrusive suites of the Tuolumne and Mt. Stuart Batholiths have ages that span between ten and five million years (Coleman et al., 2004; Matzel et al., 2006), which is longer than cooling models allow for a large single magma chamber to exist in

* Corresponding author. fax: +1 989 774 2142.
E-mail address: sven.morgan@cmich.edu (S. Morgan).

the middle to upper crust (Glazner et al., 2004). The incremental assembly model of pluton emplacement is also consistent with dike transport of magma, which is now commonly invoked as the dominant mechanism of magma ascent through the middle and upper crust (Clemens and Mawer, 1992; Petford, 1996).

The major difficulty for the incremental assembly model is the lack of evidence for individual pulses. Internal contacts are observed in only a handful of intrusions and mostly aided by differences in composition between pulses (e.g., Wiebe, 2003; Mahan et al., 2003; Harper et al., 2004; Matzel et al., 2006). Work on the Birch Creek pluton, California, has documented the presence of multiple internal contacts of generally similar composition (M. Barton, personal communication). In large, compositionally homogeneous igneous bodies, these types of contact are often not observed. It has been speculated that some internal contacts are destroyed by the emplacement of additional magma pulses or will always remain cryptic as a result of post-emplacement processes (Glazner et al., 2004; Matzel et al., 2006).

In this paper we describe and model the emplacement of a small tabular intrusion that preserves evidence for internal "sheeted" contacts. The Trachyte Mesa intrusion (TMI) is one of many small satellite intrusions in the Henry Mountains of Utah (Fig. 1). Our study focuses on both the fabric within the igneous rock and the deformation of the surrounding wall rocks. Based on contact relationships, we suggest that the TMI is exposed very close to its original emplacement dimensions, providing us with details about its emplacement not ordinarily observed at other intrusions. The unique exposure reveals a series of thin, sub-horizontal shear zones within the intrusion, which we interpret as contacts between magma sheets. Microstructures indicate that the sheets within the TMI were emplaced at very high strain rates. Using the known geometry of the intrusion along with rock magnetic fabrics, we constrain the magma flow patterns during sequential stacked sheet emplacement (e.g. Morgan at al., 2005). This model of stacking magma sheets (Morgan et al., 2005) is in accordance with one of Hunt's original emplacement models (Hunt, 1953) for intrusions in the Henry Mountains. Our data from this small intrusion clearly demonstrate emplacement processes and fabric–wall rock relationships that either do not form or are obscured in larger, more complex intrusions.

2. Geologic setting and previous work

The Henry Mountains of south-central Utah, USA (Fig. 1), provide a unique setting for the study of igneous emplacement in the shallow crust. The magma bodies intruded the Mesozoic stratigraphy of the Colorado Plateau where high elevations and a lack of vegetation allow the shape of the intrusions and the displacement of the wall rocks to be easily documented (e.g. Gilbert, 1877; Hunt, 1953; Pollard and Johnson, 1973; Jackson and Pollard, 1988; Habert and de Saint Blanquat, 2004; Horsman et al., 2005; Morgan et al., 2005; de Saint Blanquat et al., 2006). Based on $^{40}Ar/^{39}Ar$ and fission-track ages, the intrusions in the Henry Mountains are Late Oligocene to Early
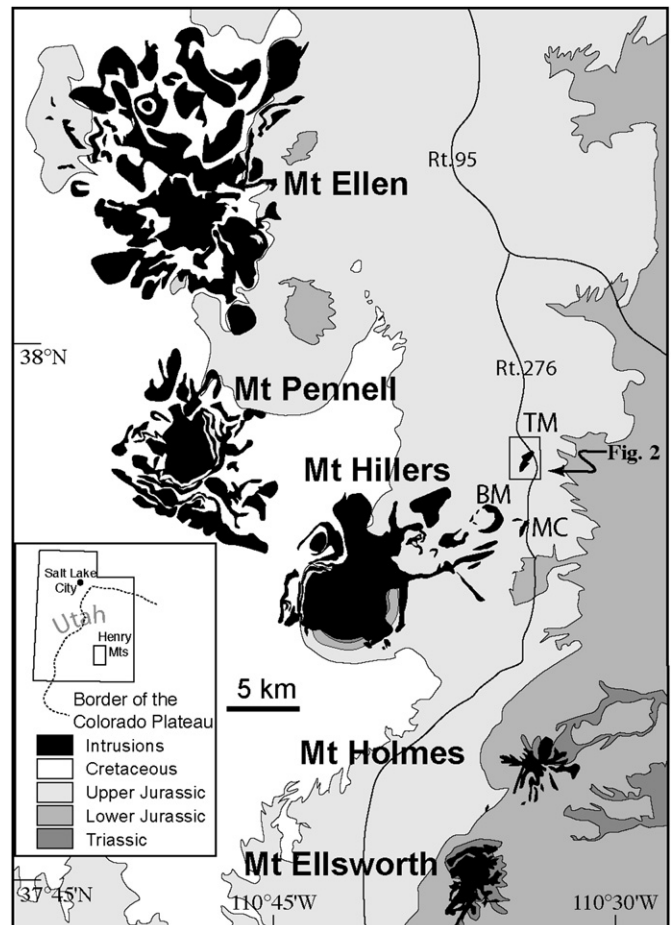

Fig. 1. Simplified geologic map of south central Utah illustrating the five intrusive centers of the Henry Mountains. TM, Trachyte Mesa intrusion; BM, Black Mesa intrusion; MC, Maiden Creek sill.

Miocene and probably part of a much broader east-west belt of magmatism that crosses the Cordillera and becomes younger to the south (Sullivan et al., 1991; Nelson et al., 1992). These intrusions postdate the minor Laramide orogenic activity that affected this part of the Colorado Plateau. Consequently, fabric within the intrusions primarily reflects finite strain produced by magmatic flow during emplacement and lacks a significant concurrent or subsequent tectonic overprint.

The range is composed of five distinct igneous centers and tens of smaller satellite intrusions that were emplaced into basically flat-lying sandstones and shales (regional dips of 1–2° west). The peaks attain heights of over 3300 m while the elevation of the surrounding flat-lying rocks of the plateau hovers around ∼1500 m. Jackson and Pollard (1988) determined that at the time of intrusion, the intrusives in the Henry Mountains were buried by 3–4 km of sedimentary overburden.

The Henry Mountains are also the "type" locality to examine laccoliths since the pioneering work of Gilbert (1877) who originated the term "laccolite" (1877) based on his observations of concordant intrusions in the region. Gilbert was one of the first to realize that magmas can deform their wall rocks and envisioned a two-stage process of magma emplacement whereby the initial intrusion is sill-like, but with continued flow of magma, vertical growth is initiated and horizontal

spreading ceases. Hunt (1953) reinterpreted the five main intrusive centers/mountains as stocks that fed the smaller satellite laccoliths, which surrounded the main intrusive centers. Hunt (1953) conceptualized laccolith growth by illustrating several models of magma chamber construction through incremental additions of magma. Further background information is given in Morgan et al. (2005).

Detailed mapping and geophysical work by Jackson and Pollard (1988) led to an interpretation more in agreement with Gilbert (1877). They concluded that the five main intrusive centers are "floored" (sedimentary rocks are found at their base) and therefore the major intrusions in the Henry Mountains are laccoliths that inflated and upwardly bent their roof rocks.

3. Trachyte Mesa

3.1. Physiography

The TMI is 1.5 km long and 0.6 km wide (Fig. 2) and varies in thickness between 5 m in the NE to greater than 50 m in the SW. The intrusion defines the top of the mesa and the edge of the intrusion is the edge of the mesa except in the SW where the margin is covered by alluvium. The long axis of the TMI trends NE and is along a line that can be traced 12.6 km SW to the peak of Mount Hillers. The top is generally flat although the NE half can be divided into three geomorphic regions (Fig. 2): (1) a long plateau on the NE margin, (2) a central plateau, and (3) a NW region which slopes down to the northwest. The central plateau is 2 to 3 m higher than the NE plateau and the border is defined by a cliff. The SW half of the intrusion is slightly more irregular in relief, has more alluvium covering the top, and rises up gently from where it is buried in alluvium to the SW.

Field observations indicate that the present exposure of the TMI corresponds closely to its original intrusive geometry, similar to many of the satellite intrusions in the Henry Mountains (e.g., Horsman et al., 2005; de Saint Blanquat et al., 2006). Many of the original igneous−sedimentary contacts are still exposed in several locations on the top and NW side of the intrusion and resemble the remaining exposed margins. This unique exposure occurs because the surrounding sandstones are poorly cemented and much less resistant to weathering than the igneous rock.

Most of the flat bottom contact is locally exposed along the walls of the mesa. Close to the top of the mesa, on the SE margin of the SE half, a 1 m thick horizontal sandstone bed separates the laccolith into a top and bottom layer. The upper and lower contact of the sandstone layer can be traced for over 10 m. Throughout the remaining portions of the intrusion, internal contacts are locally expressed by the presence of shear zones, discussed below.

The TMI has been termed a laccolith by Gilbert (1877), Hunt (1953), and all subsequent workers mentioned above. In this paper we do not use the term laccolith because the TMI has features transitional between a sill and a laccolith. The TMI is thin (most of it is less than 20 m thick) and long (1.5 km) and sheet-like and intruded parallel to bedding. At the western end of the NW margin, the intrusion does resemble a laccolith because there the intrusion is over 50 m thick and the surrounding sandstone can be seen to bend upward over the margin to become the roof.

3.2. Composition

The TMI is a homogeneous plagioclase-hornblende porphyry, similar to most of the other hypabyssal intrusions in the Henry Mountains (e.g., Hunt, 1953; Nelson et al., 1992; Nelson and Davidson, 1993). It has a microgranular porphyritic texture with euhedral phenocrysts (up to 7 mm) of hornblende and plagioclase (Fig. 3) and less commonly pyroxene and apatite. The groundmass consists dominantly of microlaths (tens to hundreds of microns) of plagioclase, weathered oxides, and micron-scale blebs of quartz, plagioclase, and potassium feldspar. Most of the hornblende phenocrysts and larger oxides were altered to finer-grained oxides and calcite. Using the total alkalis versus silica plot of Le Bas et al. (1986), the average composition based on 11 samples is dacitic.

The surrounding rock is the Jurassic Entrada Sandstone, a high porosity (porosity >10%), eolian sandstone. It is a very fine to fine-grained quartz arenite and is moderately to well sorted. The sandstone at the margins of the intrusion is largely unmetamorphosed but locally exhibits evidence for fluid infiltration. Within 50 cm from the intrusion pea-sized nodules of calcite-cemented sandstone resist weathering. These zones of calcite cement in the adjacent sandstone, together with the altered oxides, hornblendes and calcite pseudomorphs in the igneous rock, document the fluids that passed through these rocks syn- to post-emplacement (Engel, 1959).

3.3. Fabric

The fabric in the TMI is dominated by a well-defined magmatic lineation documented by the orientation of hornblende phenocrysts. Except for the thin shear zones at contacts, the large plagioclase phenocrysts are euhedral and there is no alignment of the much smaller crystals or evidence for flow or shearing in the matrix (Fig. 3). Foliation is poorly developed, except in the shear zones.

The top 2−3 cm of the intrusion is also defined by a shear zone and only observed where meter-scale blocks of in situ Entrada sandstone are preserved on the top contact. These zones are very friable and difficult to sample and mostly eroded from the top surface of the intrusion. Within the shear zones (Fig. 3a), micron-scale pieces of plagioclase crystals that have undergone intense cataclasis define the fabric, which has a much stronger lineation than foliation. The alignment of the shattered and elongated plagioclase crystals within the zone is parallel to the hornblende needles below this zone. The groundmass between the shattered plagioclase crystals exhibits no evidence for shearing and appears to be no different than the groundmass in the interior of the sheets where the phenocrysts are undeformed (Fig. 3b,c). The only exposure of the deeper parts of the interior exists very near the southern margin (see Fig. 2 for location) in a stream gorge, discussed later.
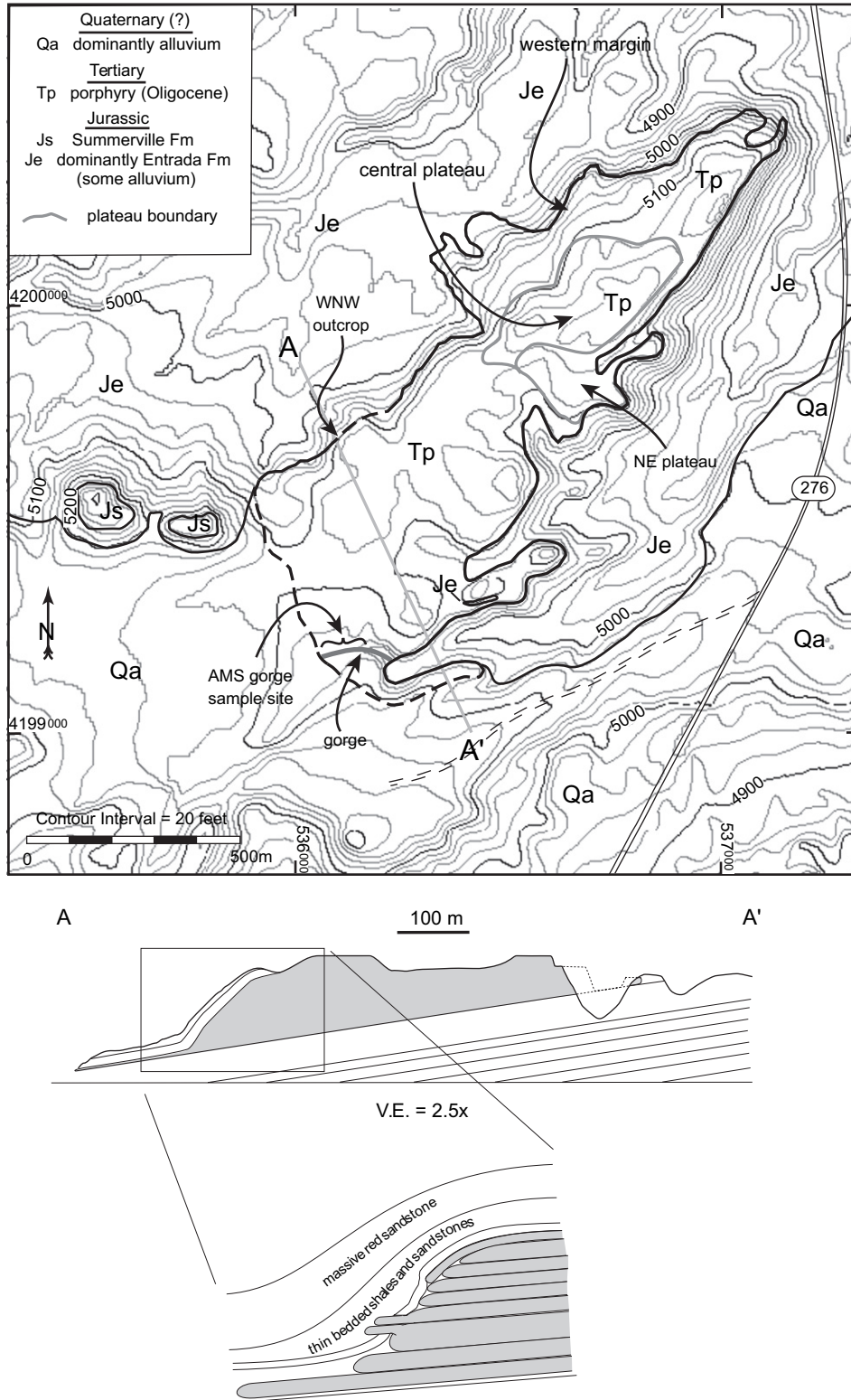
Fig. 2. Geologic map and cross-section of the Trachyte Mesa intrusion.

4. Description of the WNW Outcrop

At the western end of the northwestern margin of the mesa (Fig. 2), a complete cross section through the deformed sedimentary contact is gradationally exposed along ~100 m (horizontal distance) (Fig. 4). This is one of two locations where the sedimentary layers at the contact with the lateral margin of the TMI are preserved and not eroded or covered by alluvium. The shear zone at the contact and the outer margin of the intrusion are also well preserved at this location.
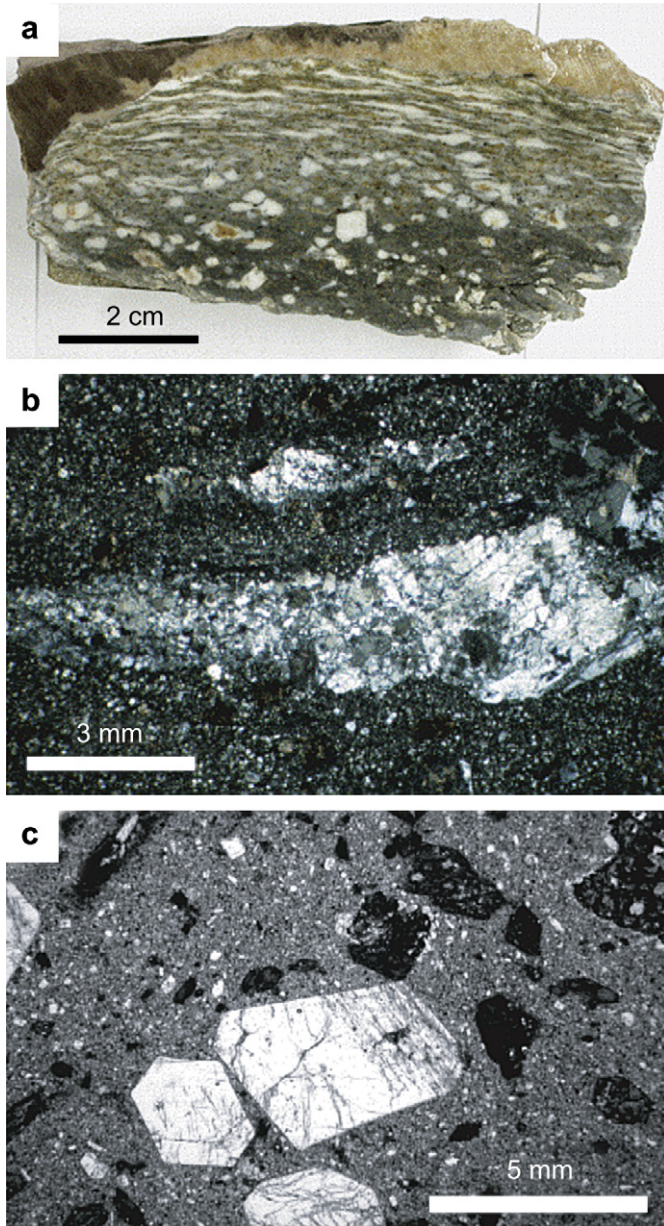
Fig. 3. Photograph and Photomicrographs of typical porphyritic dacite from the top contact and interior of a sheet. (a) Top contact of sheet with sandstone illustrating the thin shear zone and multiply faulted sandstone. White crystals are plagioclase. (b) Photomicrograph of plagioclase crystal in shear zone. Plagioclase crystals have experienced intense cataclasis and extension of pieces defines the foliation. (c) Photomicrograph of microstructure beneath shear zone. White euhedral crystals are plagioclase. Elongate crystals are hornblende and sphene which are mostly oxidized and partially replaced by calcite. Other dark crystals are oxides including magnetite and ilmenite.

As we describe in more detail below, layers of the Entrada sandstone bend monoclinally upward at the margin of the intrusion and return to their subhorizontal orientation atop the intrusion. The base of the mesa at the WNW outcrop is located at the same level where the stratigraphy begins to rotate upward, such that the base of the mesa corresponds to the lower contact of the intrusion (i.e., the stratigraphic "floor"). Our description of the WNW contact begins with the igneous rocks and continues with the deformed sedimentary sequence.
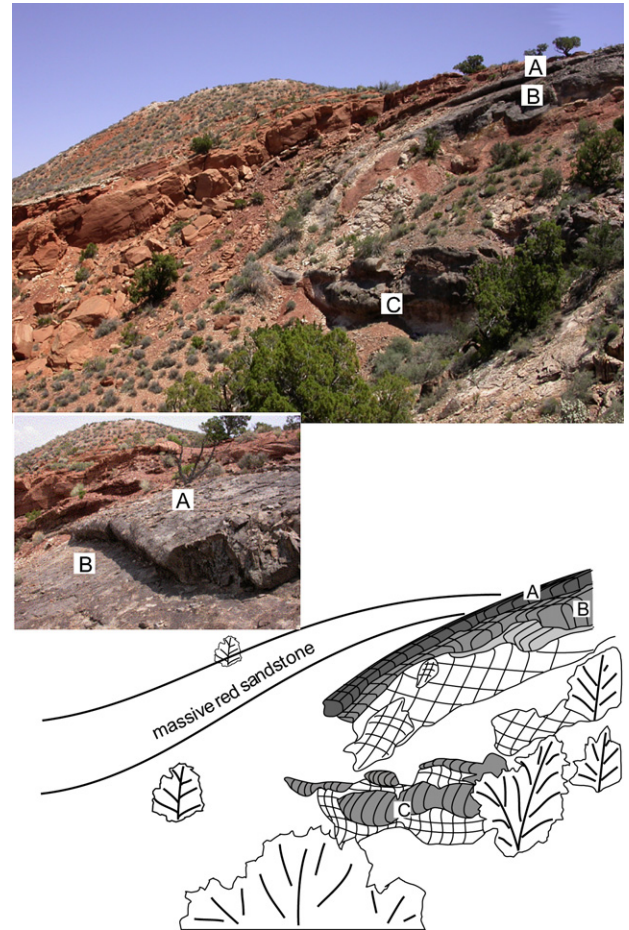

Fig. 4. Photograph and sketch of WNW outcrop, looking towards the east. Massive red sandstone of the Entrada Formation (on left) rises up over the contact to become the roof. Sill-like sheets, A, B: tongue-like sheets, C: crosshatched, clear design in the sketch are thinner bedded sandstones found below the massive red sandstone and just above the contact. The bulbous sheet to the left of the letter C is 2 m thick. Inset photo was taken at the top and is a close-up of sheets A and B. Sheet A is 50 cm thick.

4.1. Igneous sheets and internal contacts

Individual igneous sheets are identified by the shape of their terminations and the presence of 2–3 cm thick shear zones at their contacts. These shear zones are identical to those observed at the top contact of the mesa. Sheets have two distinctive shapes: (1) sill-like and (2) tongue-like. Both types of sheets have bulbous to subvertical frontal terminations. Sheet thickness varies between 40 cm and 3 m and their widths vary between 3 m and 25 m. The best-exposed sheet (sheet A, Fig. 4) defines the very top of the laccolith and mesa. This sheet is sill-like in shape and is exposed for ∼600 m² and is 50 cm thick at its termination. This sheet can be traced from the top of the mesa to the edge as it rotates 15° downward before terminating in a face sub-perpendicular to the plane of the sheet. This steep termination is also sub-parallel to the edge of the intrusion/mesa here. Beneath the termination of this sheet, two more sill-like sheets are exposed for several meters (sheets B in Fig. 4) and these continue to rotate downward towards the steep edge until they are covered by concordant sandstone

beds that dip approximately 60° away from the interior of the mesa (Fig. 4). These sandstone beds continue downward to the bottom of the mesa where they are intruded and cross-cut by tongue-like sheets (sheet C in Figs. 4 and 5). These tongue-like sheets have an average height of 1.25 m and a width of 8–10 m. They are exposed for a maximum of 5 m as they intrude through the dipping sandstones. Some of these tongue-like sheets have fault-bounded and planar margins on their sides, but the frontal terminations are often bulbous or rounded (Fig. 5).

Forty meters to the SW, a vertical sequence of stacked sheets is exposed (Fig. 6). In profile view, the terminations are rounded and convex outward so the steep outcrop appears undulated. Much of the exposure of these sheets is two-dimensional, i.e., their extent into the laccolith is not observable because all sheets basically terminate at the same lateral extent. The lower sheets protrude slightly further outward than higher sheets, resulting in a margin with a fairly steep slope (∼45°). Some of these sheets have widths of 10 m or more, but many are only several meters wide and pinch out against other sheets. The relative sequence of emplacement, determined by cross-cutting contact shear zones, can be determined in only a few places. There is not a regular vertical progression from top to bottom, or vice versa, for the order of sheet emplacement.

There are several examples where 2–4 mm wide cataclastic fault zones originate at shear zone contacts and extend outward for several meters at low angles to the contact. These minor faults have millimeter to centimeter scale offsets. These cataclastic bands are not found in the interior of these sheets. We interpret these sheets to be later than the surrounding intrusion and relate the faults to the emplacement of these sheets.

The solid-state lineation observed on the top of the sheets at the WNW outcrop trends NW, perpendicular to both the edge of the mesa/intrusion and the frontal terminations of the sheets. At the very frontal terminations of these sheets, the lineation and foliation roll-over from the top of the sheet to

Fig. 5. Photograph of tongue-like sheets (t) intruding through sandstone (ss) at the base of WNW outcrop. Dashed lines outline the borders of sheets. The sheet labeled t(c) is the same sheet labeled c from Fig. 4. The bedding of sandstone below these sheets is subvertical to steeply dipping and intensely brecciated along multiple faults.

become sub-vertical and remain parallel to the outer margin. The foliation within the interior of the sheets is observed in two locations, both within 2 m from the sheet terminus. At each location, the magmatic foliation in the interior, defined by the alignment of euhedral hornblende needles, is *perpendicular* to the top and bottom contacts of the sheet (Fig. 7). This perpendicular foliation abruptly rotates 90°, over a distance of 3–5 cm, as it approaches the top and bottom contacts to become parallel to the shear zone at the contact (Fig. 7).

4.2. Deformation in overlying sedimentary rock

4.2.1. Geometry of sedimentary layers

The WNW outcrop allows for documentation of the geometry and deformation of the sedimentary layers at the lateral margin of the TMI. A distinctive 5 m thick massive red sandstone layer of the Entrada Formation exists here and can be traced from where it is undeformed away from the intrusion to where it bends up to become the subhorizontal roof of the laccolith (Fig. 4). This bed is conveniently defined at the base and at the top by thin (<30 cm) white sandstone beds, each of which can be traced continuously at the outcrop. These white marker beds permit the thickness of the red sandstone layer to be easily measured except at the top of the TMI where erosion has removed most of it. Fig. 8 shows how bed thickness varies over a distance of 70 m from 6.0 m in the NW where it is flat-lying to 4.1 m near the top in the SE.

4.2.2. Finite strain

Two-dimensional finite strains in thin sections of the massive red sandstone (Fig. 8) were determined using the normalized version of the Fry method (Fry, 1979; Erslev, 1988). The computer program INSTRAIN (Erslev, 1988) was used by inputting the digitized positions of the long and short axis of individual sandstone grain boundaries from photographs of thin sections. Thin sections were cut perpendicular to bedding and parallel to the lineation in the contact shear zones. The coarsest grained sandstone layers were chosen for ease of grain boundary identification. Even though the coarsest grain size fraction was measured from individual thin sections (when possible), the R_s does not vary significantly (<0.1) between grain size fractions from different layers within the same thin section. Most strain analyses are based on between 200 and 400 grains taken from two areas in the same thin section, although a minimum of 100 grains per thin section were used. We utilized two-dimensional strain analyses within the massive red sandstone because there is no evidence for non-plane-strain deformation.

At the WNW outcrop, a general increase in finite strain ratios is observed from the NW to the SE as the sandstone layer bends atop the intrusion, with a drop in values at the extreme SE end (Fig. 8). No finite strain is recorded in the sandstones away from the TMI. Sandstones on the top of the laccolith, tens to hundreds of meters away from the margin, record lower finite strains than observed at the margin.
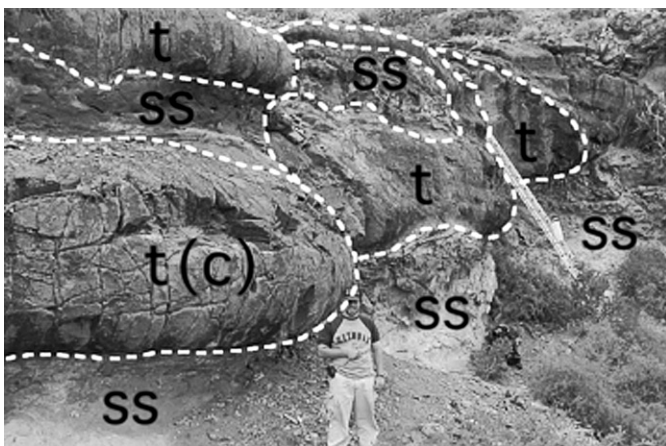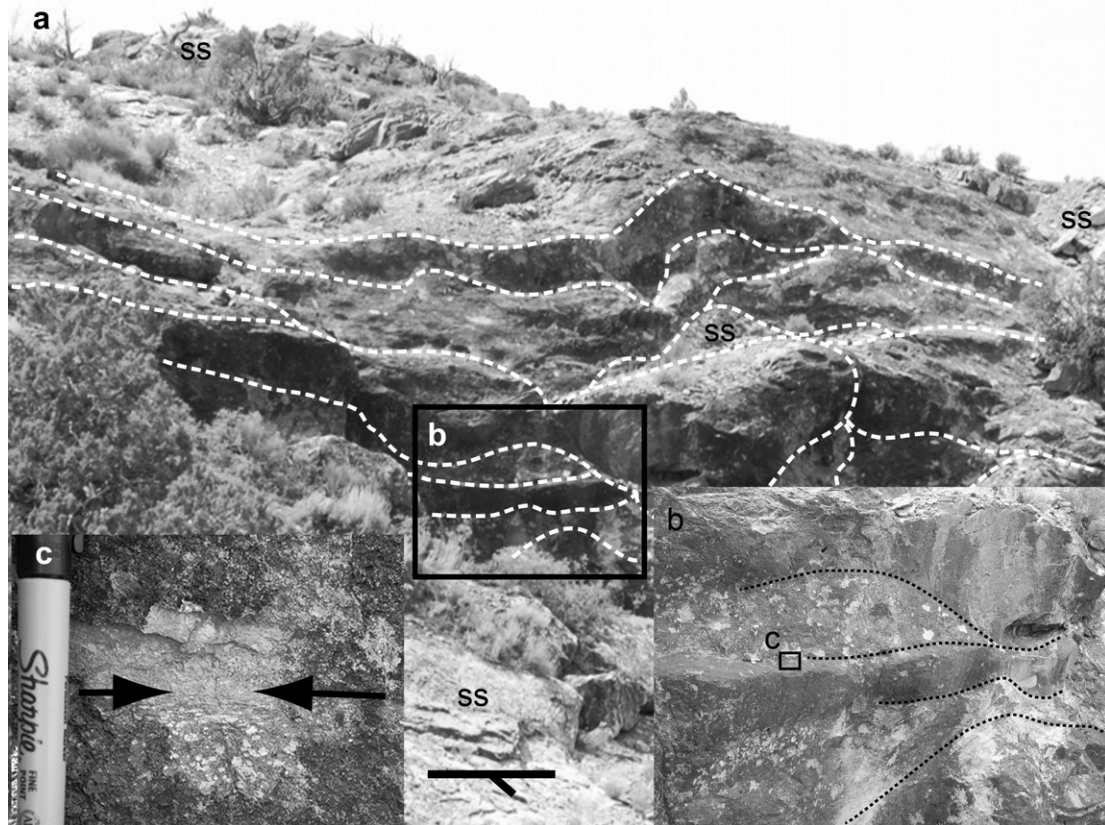
Fig. 6. Photograph of margin of the TMI revealed at the WNW outcrop. Photograph taken looking SE and outcrop is 40 m SW from the outcrop in Fig. 4. Shear zone contacts (dashed lines) separate individual sheets. SS, sandstone. Insets show details of the thin (2–3 cm) shear zone contacts.

4.2.3. Porosity

Two-dimensional porosity was measured in 23 of the samples collected from the massive red sandstone layer (Fig. 8). Grain area was traced in photomicrographs of the same thin sections used for finite strain analyses. The grain area was summed for the entire photograph and subtracted from the total area of the photograph to obtain the porosity. Four areas from each thin section were photographed for each analysis and each area contained between 20 and 40 grains. The porosity values for the four areas were averaged for a final value for each thin section/sample. Cements were not counted in the summation of grain area, and therefore our measurements represent pre-cementation porosity. Porosity generally decreases from NW to SE, although it fluctuates along the layer. The average porosity of samples 2 through 9, collected at the NW margin, is 32%. The average porosity of samples 24 through 31, collected at the SE margin, is 21%.

4.2.4. Microstructures

Grain scale deformation increases along the massive red sandstone from NW to SE. Deformation features observed in the high strain areas include: (1) fractures emanating from grain contacts, (2) grain crushing, (3) subgrain boundaries, and (4) undulose extinction emanating from grain contacts (Fig. 9). Fractures emanating from grain contacts are similar to those observed in high-porosity, experimentally deformed sandstones. "Cone crack" patterns (Zhang et al., 1990) are common and indicate stress concentrations at grain contacts. The majority of microfractures do not cross from grain to grain. Completely crushed grains are typically found in between large grains (Fig. 9). Calcite cements are heterogeneously deformed. Some intergranular calcite is undeformed, while elsewhere it is highly cleaved and fractured in an irregular fashion.

4.2.5. Faulting

High-angle faults with millimeter to centimeter scale offsets are common in the sedimentary rocks in the southeastern Henry Mountains region (Davis, 1999) and are also observed within the massive red sandstone sequence that arches up over the TMI. The faults are typically concentrated within a single bed and appear in conjugate sets with similar strikes and opposing high angle dips.

However, in the sedimentary layers that rise up over the TMI, en-echelon cm-scale shear fractures occur in planar zones that cut-across all high-angle faults (Fig. 10). The fractures in these zones erode more rapidly than the surrounding rock leaving planar indentations and bleached zones. These planar zones dip towards the interior of the laccolith and normal offset is always observed across them. These zones *only* occur in the massive red sandstone layer where it has been arched upward over the margin of the TMI (Fig. 8), and therefore are most likely related to the emplacement of the TMI.
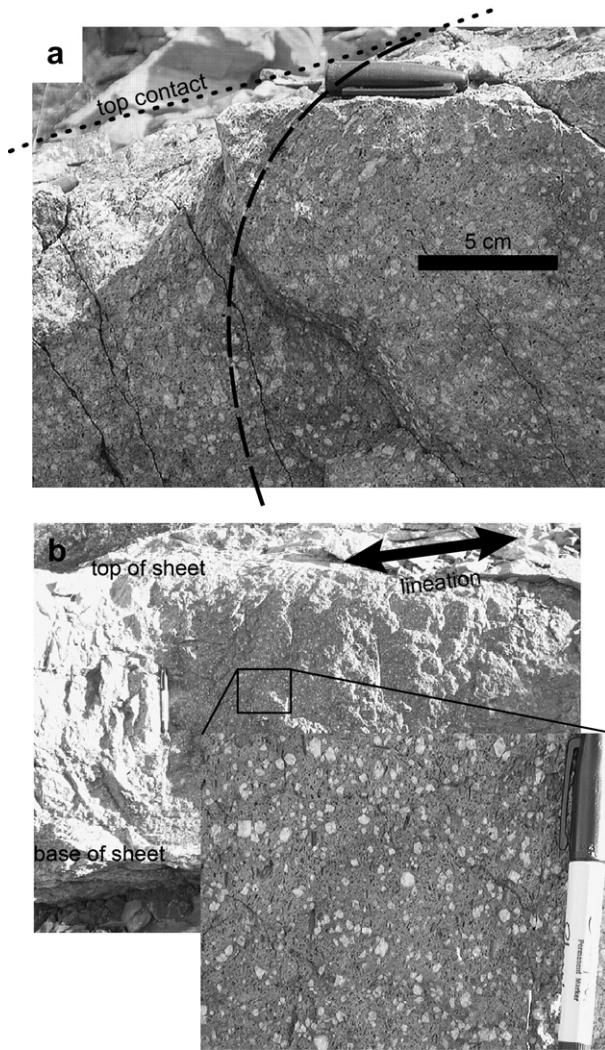
Fig. 7. (a) Photograph of top contact of sheet B from Fig. 4. Dotted line: top contact, which is partly eroded away. Dashed line: curvature of foliation. (b) Photograph of foliation in sheet A from Fig. 4. Foliation in the interior of the sheet is parallel to the pen and perpendicular to the top and bottom contact.
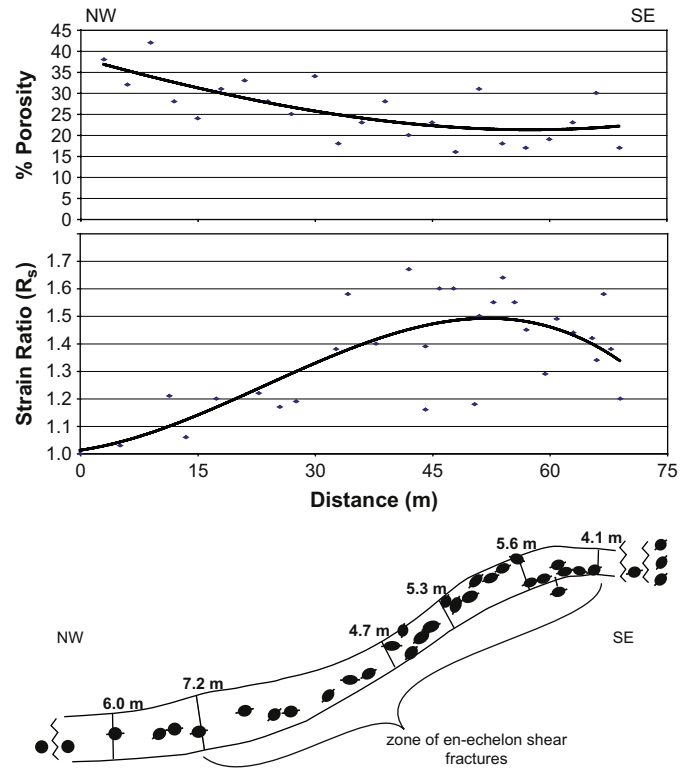

Fig. 8. Measurements of thickness, finite strain, porosity, and sample locations along the massive red sandstone bed at the WNW outcrop. Strain ellipses and strain ratios based on normalized Fry analyses. Curves are best fit third order polynomials ($R^2 = 0.56$ for strain ratio curve and 0.49 for % porosity curve). See text for details.

Stratigraphically below the massive red sandstone is a 2-m thick package of sandstone and shale beds that has been highly faulted and sheared. Reverse (thrust) faults, with up to 20 cm of offset (Fig. 10) are common. Faults are also observed along these sedimentary contacts. The sandstone layer at the contact contains large (>50 cm) angular to rounded blocks of sandstone in a matrix of largely incohesive sand (Fig. 10d) and is classified as a megabreccia.

4.2.6. Sedimentary–igneous contacts

Locally, the contact between the sedimentary sequence and the igneous sheets includes a mixed zone, up to 25 cm thick, of sandstone and igneous rock that is intensely foliated and sheared (Fig. 10e). The shear sense based on shear bands within this foliated zone is consistent with the outward motion of sheets directly below.

Intensely faulted sedimentary rock occurs in remnants around the edges of all sheets and directly below the tongue-

like sheets that intruded through the inclined sandstones at the base of the mesa discussed earlier (Fig. 5). Examination of these rocks suggests that multiple periods of faulting occurred at different orientations. Bedding in these sandstones is subvertical to steeply dipping away from the TMI. Note that the orientation of bedding in these thinly (<1 m) bedded layers, which are stratigraphically below the massive red sandstone and which are in direct contact with sheets at the WNW outcrop, is significantly steeper (70–90°) than the bedding in the massive red sandstone (steepest dip is 30°, see Figs. 4 and 5). Our emplacement model explains the significance of these data and is discussed later.

5. Anisotropy of magnetic susceptibility (AMS)

5.1. Magnetic carriers

Measurement of the anisotropy of magnetic susceptibility (AMS) in igneous rocks provides a proxy for the shape orientation (petrofabric) of the minerals and is commonly used to infer the flow of magma in an intrusion (Bouchez, 1997 and references therein). AMS is approximated by a symmetric 2nd rank tensor, represented by an ellipsoid with three principal axes ($K_1 \geq K_2 \geq K_3$). The long axis of the ellipsoid is generally aligned parallel to the flow direction while the short axis is the normal to the magma flow plane (Bouchez, 1997). The
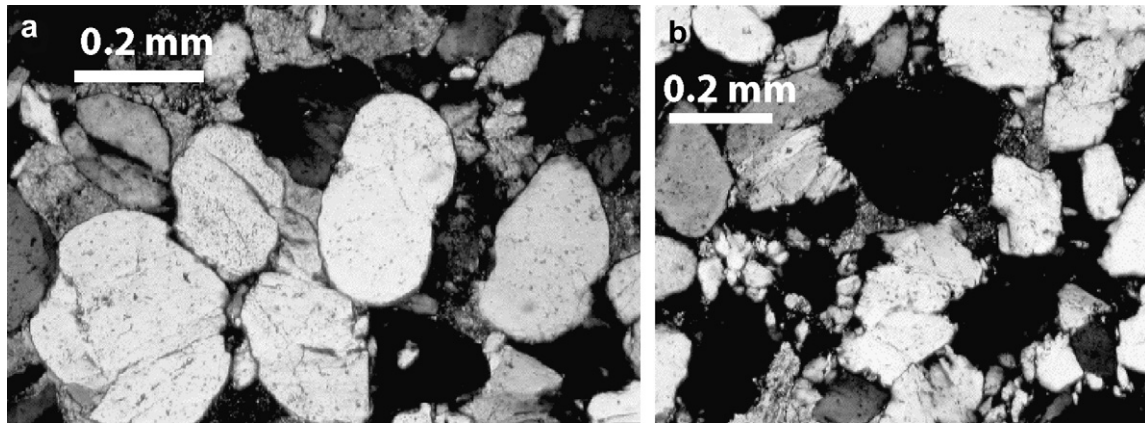
Fig. 9. Photomicrographs of fractured quartz grains illustrating the brittle deformation observed within the massive red sandstone. See text for details.

AMS signal in ferromagnetic rocks is dominated by magnetite because of its intrinsically high susceptibility, even though its anisotropy (difference between K_1 and K_3) is very low. The AMS ellipsoid is dominantly controlled by the shape-preferred orientation of individual crystals of magnetite, or of clusters of magnetite (Grégoire et al, 1995; Gaillot et al., 2006). The magnetic properties of a rock are attributed to magnetite when it is present in proportions greater than $\sim 0.5\%$ of the iron oxide fraction (Tarling and Hrouda, 1993). Problems with the petrofabric interpretation arise when other minerals comprise more of the iron oxide fraction, which can happen with weathering or with the production of secondary magnetite during late fluid circulation (de Saint Blanquat et al., 2006). The magnetic grain size is also important because single domain (SD) magnetite can result in inverse fabrics (K_1 and K_3 axes are reversed, see Rochette et al., 1992; Tarling and Hrouda, 1993). Therefore, optical inspection of the magnetic carriers and detailed testing of the magnetic mineralogy and domain size were conducted.

Saturation isothermal remanent magnetization (SIRM) and alternating field (AF) demagnetization were done on two samples to produce cross-over plots (Symons and Cioppa, 2000). Both plots indicate that magnetite is behaving as pseudo-single domain and that the total magnetic signal is controlled by magnetite along with another magnetic phase. Curie temperature analyses on two samples confirm the presence of magnetite and possibly some other minor phase. Hysteresis loops on five samples indicate that the magnetic crystals are behaving as pseudo-single domain and multi-domain grains. In thin section, two grain sizes of oxides are visible: fine grains in the matrix, and coarse subhedral clots in the matrix and along cleavage planes in heavily altered amphiboles. Energy Dispersive Spectrometry (EDS) with an ARL-SEMQ electron microprobe reveals that the coarsest grains are mostly ilmenite or highly titaniferous magnetite, and the smaller grains in the groundmass are slightly titaniferous to almost pure magnetite. The coarser generation of oxides may be related to a late fluid expulsion from the final crystallization of the magma, similar to observations in the nearby Black Mesa intrusion (de Saint Blanquat et al., 2006). Although

the magnetic mineralogy is complex, the macroscopic fabric, especially the well-defined field lineation consisting of horn-blende needles, is always parallel to the magnetic lineation (K_1). Based on our analyses and observations, we interpret the AMS fabric to be representative of the rock fabric, similar to work in the adjacent Maiden Creek intrusion (Horsman et al., 2005).

5.2. Results

Samples analyzed for AMS were collected from 103 locations on the top surface of the TMI and 73 locations from a subvertical cliff in a stream gorge that cuts through the intrusion's southern margin. The bulk magnetic susceptibility (K_m) varies between 0.23×10^{-3} and 12.1×10^{-3} SI, with the average at 8.3×10^{-3} SI (Appendix A). The average magnetic anisotropy $P\%$ (defined as $((K_1/K_3) - 1) * 100$) is 2.75%. These values are much higher than samples from the Black Mesa intrusion (mean of 1.8%, de Saint Blanquat et al., 2006), located 3 km to the SW, but similar in magnitude to samples from the Maiden Creek sill (Horsman et al., 2005), 3 km due south (Fig. 1). There is a slight increase of $P\%$ with increasing K_m (Fig. 11) and the shape parameter T is dominantly oblate (Fig. 11). The scalar AMS data from samples collected on the top surface, versus the cliff along the gorge, have slightly higher median values for K_m (8.47 vs. 8.08×10^{-3} SI) and $P\%$ (2.8 vs. 2.68), although the shape parameter T is the same (0.20).

The map of the magnetic lineations from the top surface of the intrusion is shown in Fig. 12. Foliations are sub-horizontal across the entire top surface. All lineations plunge very shallowly. Along the center and oriented parallel to the long axis of the TMI, there is a ~ 100 m wide zone in which the lineations are strongly concentrated and trend NE. The lineations away from this central zone are sub-perpendicular (NW and SE) to the lineations within the central zone and fan outward toward the margins. In the SW half of the intrusion the central zone is much wider and trends more to the east as it crosses the top surface. Lineations outside this zone are also sub-perpendicular to the zone. The plateaus on the top
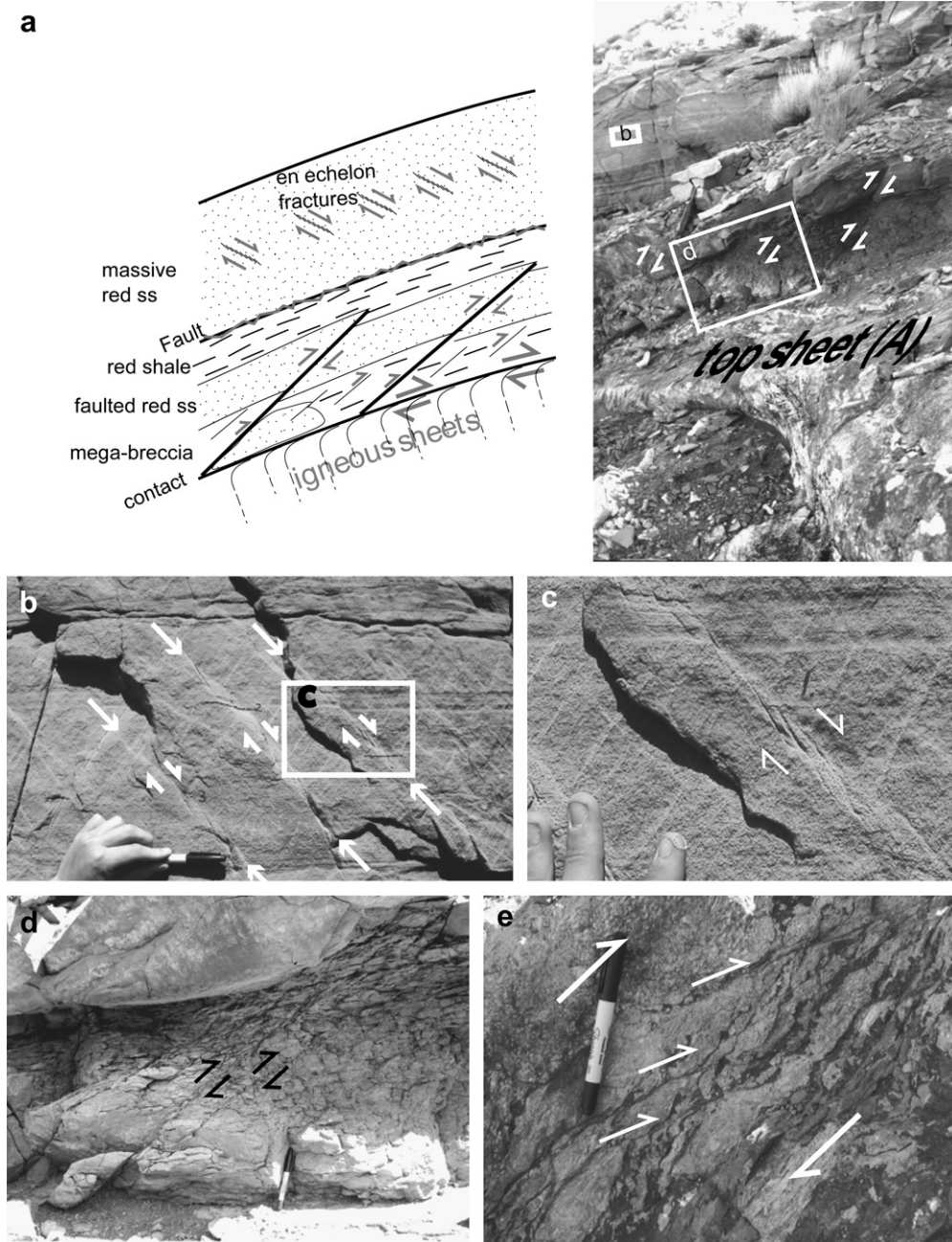
Fig. 10. (a) Sketch and photograph of deformation in sedimentary layers at contact at WNW outcrop. (b) Close-up of en-echelon shear fractures in massive red sandstone. (c) Close-up of fractures in b. Note the high angle faults which are cross-cut by the shear fractures. (d) Megabreccia of sandstone layer at contact, which is approximately 55 cm thick. See photograph a for location. (e) Shear bands in mixed zone found locally at contact.

of the TMI are also defined by differences in trends of the magnetic lineation. The lineations in the central plateau trend to the NE, whereas the lineations in the NE plateau trend to the ESE (Fig. 12).

The AMS samples collected from the cliff face in a stream gorge were collected along 11 vertical traverses (Fig. 13). The gorge cuts through the southern edge of the exposure (Fig. 2) where the TMI is mostly buried beneath alluvium. Although the base of the intrusion is not exposed here, it is observed 200 m to the NE. If this shallowly dipping lower contact is projected back to the gorge as a planar surface, it lies only

a few meters below the bottom of the stream bed. The top contact is marked by sandstone and rises gently to the east. Therefore, we assume that this part of the TMI is very close to the original SW termination of the intrusion. The 73 AMS sites from this gorge reveal a strongly concentrated subhorizontal foliation and ESE trending lineation. These lineations are consistent with the magnetic lineations collected on the top surface nearby. Fig. 13 also shows the anisotropy data (*P%*) for each traverse with the data scaled to the relative high and low mark along that traverse. No internal contacts were observed.

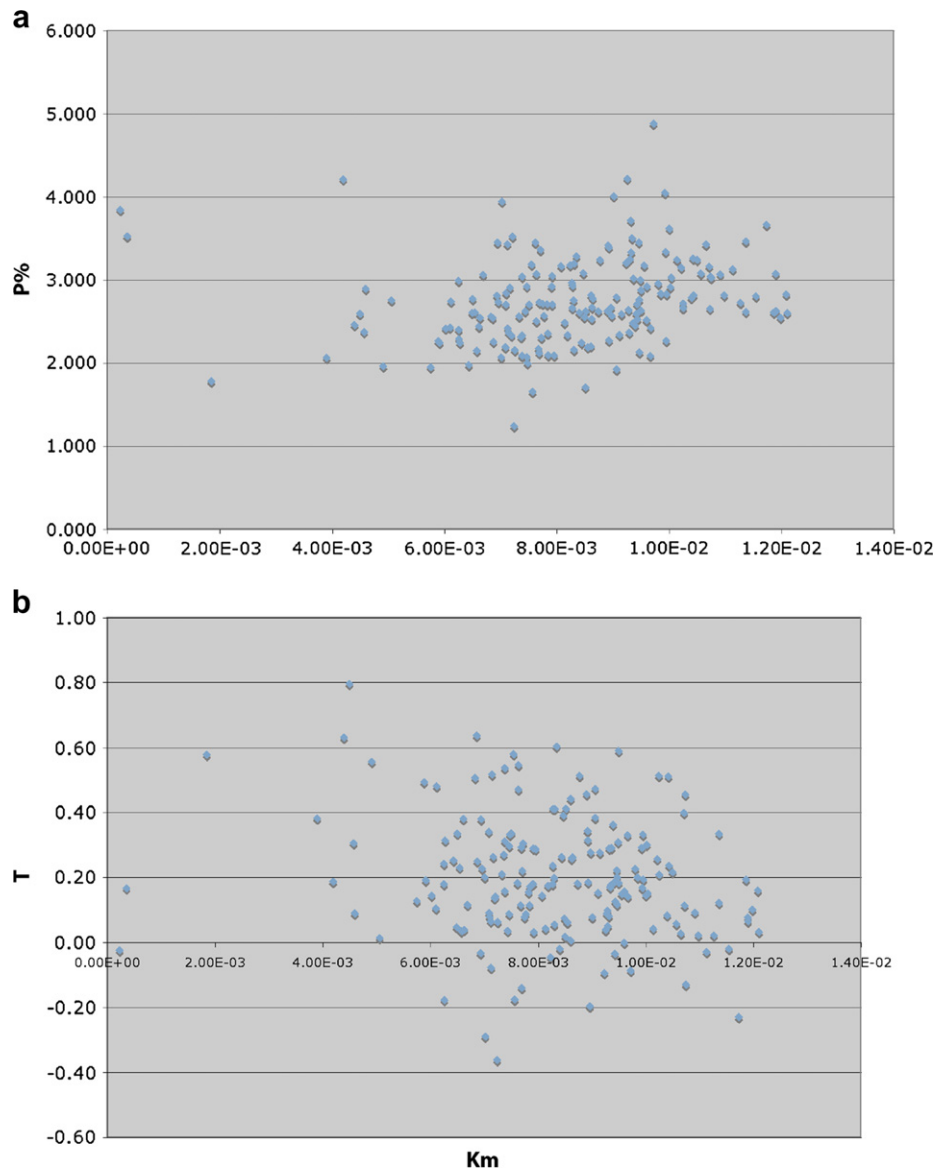Fig. 11. AMS scalar data plots. (a) Mean susceptibility, K_m versus degree of anisotropy, $P\%$. (b) Mean susceptibility, K_m versus shape factor, T.

6. Discussion

6.1. Sheets

We interpret the thin, planar, sub-horizontal shear zones observed at several locations to represent the boundaries between individual magma sheets. The degree to which the shear zone contacts extend into the interior of the intrusion, and therefore the degree to which individual sheets exist into the interior, is unknown. Field evidence indicates that these contacts exist for at least 30 m into the interior based on the extent of the sheets at the cross-section outcrop.

Additionally, individual sheets may exist across the entire width of the TMI. The magnetic data from the central and NE plateaus, along with their physiographic distinctions, suggest that these plateaus represent distinct sheets, which moved in different directions and were emplaced at slightly different times. Therefore we suggest that many sheets probably exist

on the top, as evidenced by unique geomorphic areas atop the TMI with uniquely oriented lineations.

Along the walls to the stream gorge there is a lack of shear zone contacts although there is still some evidence for internal contacts expressed in the scalar AMS data. The $P\%$ data (anisotropy) from the walls of the stream gorge (Fig. 13) fluctuate in a somewhat regular fashion from traverse to traverse and possibly define individual sheets if higher values represent contacts. In T1 through T8 in Fig. 13, every traverse has either three or four peaks and the highest value of $P\%$ is at or near the bottom of each traverse. These "sheets", as defined by peaks of $P\%$, would be 2 to 4 m thick, consistent with the thickness of sheets observed at the cross-section outcrop. The reason for the lack of shear zone contacts in the gorge, if individual sheets exist in the gorge, may be because this part of the intrusion was hotter and cooled more slowly than the lateral margins, making both formation and preservation of distinct contacts less likely.
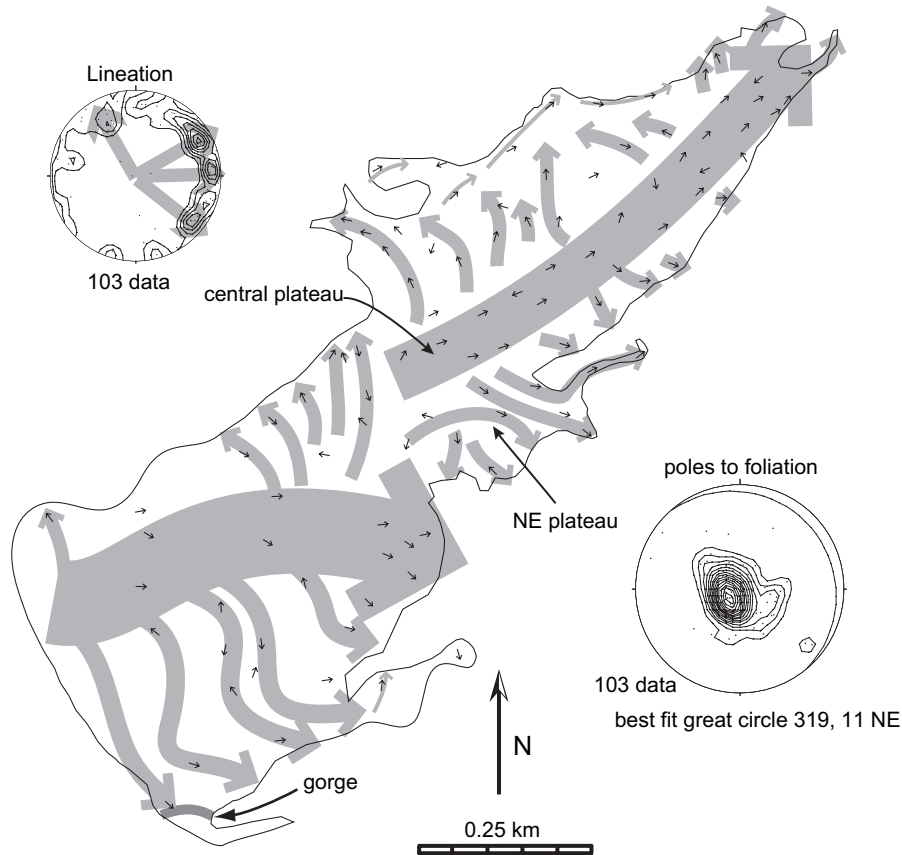
Fig. 12. Map of the AMS lineations from 103 sites on top of the TMI. Shaded areas are the author's interpretations of magma flow paths.

Alternatively, the stream gorge outcrop may represent one thick sheet or fabrics may have formed in response to flow conditions different than at the cross section outcrop. The margin at the SW edge of the TMI is very different than the other margins in that the slope to the margin is very shallow (<10°, see Fig 13). The sandstones at the top contact gradually rise over several hundred meters, defining a wedge shape versus the sub-vertical margins on the other three sides. The

significance to this wedge shape is discussed later, after the flow directions in the magma are interpreted.

6.2. Interpretation of magnetic fabrics

The trend of the magnetic lineation is commonly interpreted as the direction of maximum stretching of the magma produced by flow. If a simple shear history is assumed, the
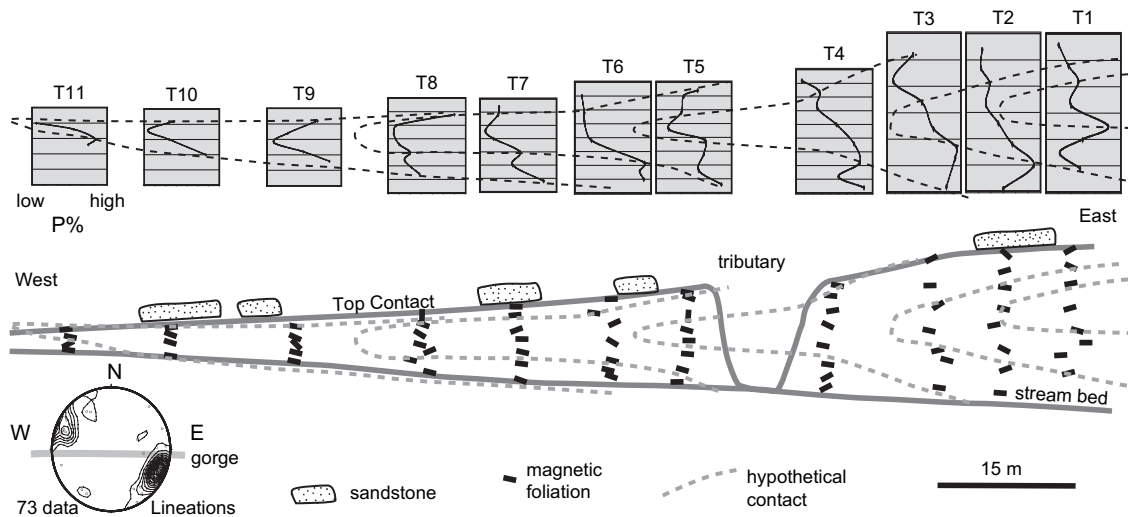
Fig. 13. Map of the AMS foliations from 11 vertical traverses along the cliff-face from the gorge that cuts through the southern corner of the TMI. Profiles are the normalized variation in P% with depth from the traverses. Hypothetical contacts drawn based on connecting highs in P%.

direction of magma flow within the sheets is parallel to the local magnetic lineations. At the WNW outcrop, the uppermost igneous sheets are exposed along a few vertical faces oriented parallel to the magnetic lineation. The shallowly plunging magnetic lineations, observed over the entire top of the TMI (Fig. 12), can be understood by examining these vertical faces. When viewed along these faces, the sheared fabric at the top of the sheet is parallel to the top contact. 2–3 cm below the top of the sheet, the fabric rotates abruptly to become sub-perpendicular (Fig. 7). The sense of motion from the curvature of the fabric is that the foliation has been dragged from its subvertical position in the interior of the sheet to subhorizontal by frictional forces with the overlying sandstone as the magma sheet moved underneath the layer of sandstone. The curvature of the foliation is consistent with motion of the magma sheets away from the central portion of the laccolith and towards the edges.

If this outcrop is typical of emplacement of magma sheets within the TMI, the top surface of the TMI should be characterized by a slightly inclined foliation and a lineation that plunges in the direction in which the sheet traveled. Examination of the directional AMS data from the top of the TMI shows that the dominant magnetic lineation trends to the NE (Fig. 12). The best fit great circle to the poles of the magnetic foliation dips 11° down to the NE (Fig. 12). The dominant magnetic lineation lies in this plane and is oriented parallel to the direction of steepest dip (NE) of the foliation plane. We suggest that this foliation and lineation are part of the same curved fabric that is described above for the sheets at the WNW outcrop. Therefore the top surface of the TMI is exposing this curved foliation very near the top contact and this inclined fabric suggests that for the most part, the magma moved from SW to NE.

6.3. Magma flow

Most of the sample locations with NE trending lineations are found in a narrow NE trending zone located along the central axis of the intrusion (Fig. 12). We interpret this zone as a primary transport channel for magma traveling from SW to NE in the uppermost sheet. The trend of the lineations outside of this zone are rotated away from the long axis and these are interpreted as secondary magma channels that grew outward from the main channel, and post-date the main channel. This is the process we envision for the lateral growth of sheets from fingers (Fig. 14). The exact details of this transformation from main channel to marginal sheets are unclear. We favor a model whereby finger or tongue-like sheets emanate and coalesce to become wider sheets but the pattern of the lineations are also consistent with wide sheets emanating from the primary transport channel (Fig. 14). Tongues can be seen on both the SE and NW margins of the TMI (Fig. 2) that possibly failed to expand into sheets and the very NE tip has two small fingers shaped like pincers. Fingers are also observed branching outward from the Maiden Creek sill, (Fig. 1; Horsman et al., 2005) and the Shonkin Sag laccolith in Montana (Pollard et al., 1975). Additionally, detailed three-dimensional seismic reflection studies of shallow sills demonstrate similar lobes branching away from central axial feeders (Thomson and Hutton, 2004; Hansen and Cartwright, 2006).

The SW half of the TMI may have been emplaced in a similar manner, although the primary magma pathway is wider and of slightly different orientation (Fig. 14). We assume that the SW half of the TMI is older simply based on the direction the magma traveled in the two halves and we assume
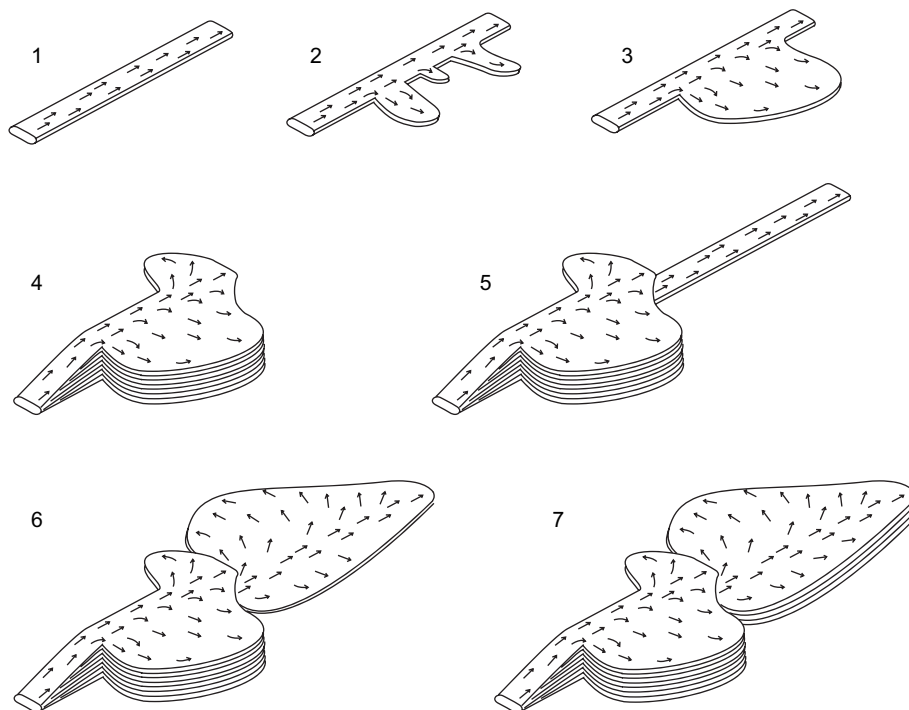

Fig. 14. Schematic time series illustrating model of emplacement of magma sheets from initial magma channels.

that the SW half fed the NE half. The magma flow indicators suggest that the TMI was fed from a source to the SW, which may be a feeder-pipe or sill emanating from Mt. Hillers. These flow directions are also consistent with the interpretation, based on the shallow slope to the top contact at the SE margin (seen in the gorge site), that the SE margin is the contact where the magma is entering into the intrusion. The wedge shape to the contact may be a response to greater thickening of the intrusion further to the NE, through the addition of sheets coming off the main channel.

The subvertical nature of the fabric within the interior of sheets is only observed within a few meters from the frontal termination, but nevertheless is unusual. In order to explain this pattern, we refer to the physical modeling of Kratinová et al. (2006) where a similar fabric pattern was observed at the front of a sheet-like model intrusion. In their experiment, colored layers of wet plaster of Paris embedded with magnetite particles were forced upward through a hole and into loose sand by pressing down on the surrounding sides of the hole. The resulting intrusion was tubular, but in two-dimensions resembles a sheet (Fig. 15). It should be noted that during the emplacement of the plaster of Paris, the model of Kratinová et al. (2006) was oriented so that the intrusion grew vertically. We have rotated their experiment by 90°, so that the plaster of Paris intrusion is in the same reference frame as sheets at the TMI.

After intruding into the sand, the plaster intrusion was dried, cut into half, and sampled for AMS fabrics. The magnetic foliations just beyond the feeder hole are parallel to the contacts and parallel to the transport direction of the

"magma". Beyond this zone the foliations rotate 90° to become perpendicular to the transport direction. By analogy, we interpret the flow in the sheets at the WNW outcrop to be similar to the flow in the front of the wet plaster of Paris intrusion. The fabric rotation in the Kratinová et al. (2006) model occurs where the magnetic strain switches from prolate to oblate (Fig. 15). The prolate fabrics are found where the model intrusion is forced through a hole and just beyond the hole, where the flow is constricted. The oblate fabrics form beyond this region and extend to the front of the intrusion. We suggest this rotation in fabric occurs because it is the region where the flow changes from being constricted to where it is diverging (i.e., spreading outward, away from the center). Examination of Fig. 15 illustrates how the limbs of the shaded plaster of Paris layer, which is folded isoclinally, begin to separate from each other at the same distance from the entrance hole that the fabric begins to rotate, supporting the hypothesis that the switch in fabrics is caused by a change in the flow regime from constrictional to divergent.

The modeling of Kratinová et al. (2006) also supports our use of the fabric on the top of the TMI as a magma "flow sense" indicator. Near the termination of the model intrusion (left half), the orientation of the foliation rotates from margin-perpendicular (subvertical in Fig. 15) within the interior to being subparallel (subhorizontal in Fig. 15) at the top and bottom, presumably as a result of frictional drag with the surrounding sand as the intrusion advanced. Note that the foliation has not rotated completely into being margin parallel and is slightly inclined. Therefore, on the top margin of the model intrusion, the foliation dips in the direction that the intrusion advanced and can be used as a flow sense indicator. This is true even in the zone where the foliations are parallel to the margins (the right half of the intrusion in Fig. 15).

This slight inclination to the foliation observed along the long edges of the model intrusion is consistent with the shallow inclination to the foliation observed across the top of the TMI. The best fit great circle to the poles to the AMS foliations collected across the top of the TMI dips shallowly (11°) to the NE (Fig. 15). A NE transport direction is consistent with our model whereby the magma that fed the intrusion originated from Mt. Hillers, which is located approximately 12 km to the SE.

The foliation pattern along the walls of the stream gorge can also be interpreted using the model of Kratinová et al. (2006). In the experimental model, the subvertical foliation is restricted to the region near the front of the sheet, and behind this region, the foliation is parallel to the margins, similar to the foliation in the stream gorge. Assuming the magma was flowing parallel to the magnetic lineation recorded in the stream gorge, the stream gorge is exposing part of a sheet that is several hundred meters away from its frontal termination based on the map of the magnetic lineations (Fig. 12). Therefore, we should expect to see horizontal foliations at this location, and at all locations in the interior, because only near the frontal terminations to the sheets will the foliations be subvertical.

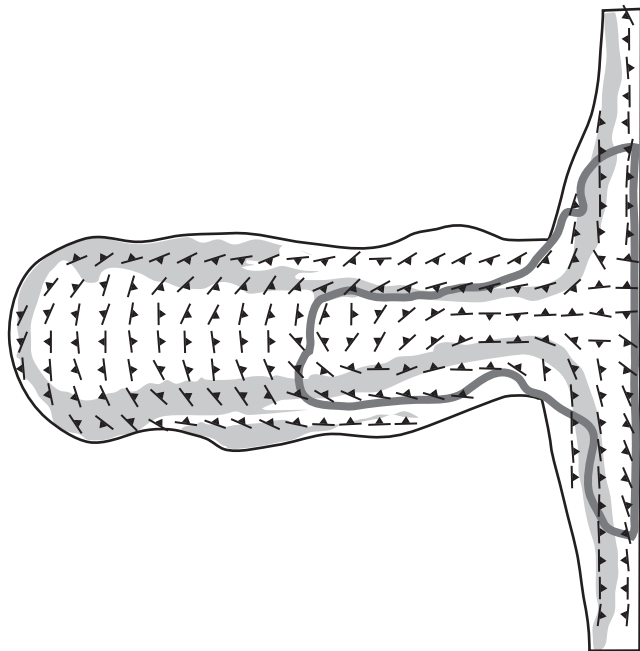Fig. 15. Results from the physical model of Kratinová et al. (2006). Sketch illustrates the orientation of the AMS foliations from samples taken from a cross-section through the center of the model intrusion. Light shaded region represents the original colored layer in the model. Dark shaded line indicates the area where prolate strains are found. Outside of this area oblate strains are found. After Kratinová et al. (2006).

The subvertical foliations near the front of the sheets are also suggestive of plug flow. The increasing viscosity of the TMI magma sheets as they traversed away from the main channel and cooled may have caused the rheology to become non-Newtonian, leading to plug flow, similar to numerical modeling results for flow in volcanic conduits (Gonnermann and Manga, 2003). We interpret emplacement of the sheets at the WNW outcrop as a form of plug flow for two reasons: (1) the interior of the sheets is defined by a sub-vertical alignment of elongate crystals which is an unstable orientation if this zone was undergoing progressive horizontal simple shear (Arbaret et al., 1997), and (2) the foliation abruptly curves at the upper contact to become subhorizontal, as predicted in high strain, subhorizontal shear zones. Therefore only the margins of the sheets are affected by the shearing.

Non-Newtonian, Bingham rheology (yield strength) and plug-flow have been proposed for various magmatic and lava flows within dikes, sills, and channels (Komar, 1972; Cigolini et al., 1984; Ross, 1986; Kilburn and Guest, 1993; Harris et al., 2002). Once the magma is flowing as a plug, the strain rate increases exponentially because all the shearing is concentrated in the narrow contact shear zone (whereas initially the shear strain was distributed across the entire sheet). This jump in strain rate at the margins probably resulted in the cataclasis of the plagioclase crystals in the contact shear zones.

6.4. Deformation at the margins

The correlation between the location and types of strain and the position of the margin of the laccolith suggests that the deformation in the sedimentary rocks in the WNW outcrop is a result of the emplacement of the TMI, except for the pre-existing, small displacement (<1 cm), high angle faults in the massive red sandstone. The strains can be partitioned into extensional and layer-parallel shearing components that are assumed to have operated simultaneously. The extensional component, or layer-parallel elongation, is the consequence of vertical stretching of the wall rocks at the margins of a vertically thickening intrusion and is documented by the thinning of the massive red sandstone as it rises up over the TMI and supported by the strain analyses and en-echelon normal sense fractures. The shearing component, as well as some component of layer-parallel shortening, is documented by the thrust faults within the layers beneath the massive red sandstone, the faults parallel to the sedimentary bedding, and by the shearing of the mixed zone at the contact. The shearing and layer-parallel shortening at the contact is probably a consequence of the motion of underlying sheets with some degree of coupling at the contact.

6.4.1. Extensional component

Within the massive red sandstone, the most intense thinning occurs at the very SE margin of the exposure, although the thickness of the sandstone was difficult to measure there. Throughout the rest of the massive red sandstone layer, the thinning is directly related to bulk strain within the sandstone.

The normalized Fry analyses produce strain ratios which are greatest ($R_s = 1.67$) at a distance of 43 m from the NW margin (Fig. 8), which is also the location of the greatest amount of thinning (neglecting the measurement at the very SE margin). On a larger scale, the overall change in strain ratios from NW to SE correlates broadly with the change in thickness of the massive red sandstone layer. In general, strain ratios increase from NW to SE as the bed thins, are highest where the bed is thinnest in the middle portion, and decrease as the bed increases in thickness to the SE.

The strain determined by the Fry analyses is consistent with the amount of thinning determined by measuring the changes in thickness of the massive red sandstone layer. A strain ratio (R_s) of 1.6, which is close to the maximum ratio calculated for the layer between 40 and 55 m (Fig. 8), indicates a shortening perpendicular to the long axis of the strain ellipse of 21%. If we assume the layer started out with a constant thickness of 6 m and shortened to a minimum of 4.7 m, a shortening of 22% is recorded. This result indicates that the faulting found throughout the massive red sandstone is accommodating little, if any, of the thinning.

Another important relationship between emplacement and deformation within the wall rocks is the inverse correlation between porosity and strain. There is some variation in the data, although the best-fit curves (Fig. 8) highlight a significant decrease in porosity, from NW to SE as the strain ratios increase. Our interpretation is that the bulk strain is a result of porosity collapse as the laccolith grew vertically and stretched the sandstone layer over the margin. Given the intense amount of fracturing observed in thin section in the samples from the most attenuated part of the section, we suggest that grain fracturing allowed for increased grain boundary sliding and grain rotation. These cataclastic processes resulted in pore collapse as finer grains moved into pore spaces. This effect was observed in rock deformation experiments on high porosity sandstones (Zhang et al., 1990). This case is unique in that we can document pore collapse across an entire stratigraphic bed, as most pore collapse in high porosity sandstones has been documented on centimeter-scale fault zones (e.g., Shipton and Cowie, 2001).

Three samples of the wall rock, collected on the top of the TMI and 160 m from the margin, all exhibit evidence for intense strain. In contrast, the sandstone is unstrained beyond the boundaries of the TMI. These data indicate that although the roof is relatively flat, it was still deformed by the emplacement of the underlying sheet.

The orientation and normal-sense offset of the en echelon shear fractures is also consistent with thinning and extension of the massive red sandstone. We interpret that these shear fractures formed in response to uplift and extension during emplacement because they consistently offset the high angle faults, which are believed to have formed prior to emplacement of the TMI, and because they are only found where the massive red sandstone is rotated upward.

6.4.2. Shearing component

The high angle reverse faults found in the layers just above the contact (Fig. 10) have the same sense of shear as the

en-echelon faults discussed above, although the orientation of these faults indicates they accommodated thrust motion, or layer-parallel shortening. Layer-parallel shortening adjacent to the contact is difficult to reconcile with the layer parallel extension in the overlying massive red sandstone, especially because both kinds of deformation occur synchronously with emplacement. This contrast in strain accommodation may be resolved by examining the megabreccia immediately above the contact, as well as the sheared mixed zone commonly found along the contact. These structures attest to the intense shear strain the contact experienced during emplacement of the underlying sheets. Therefore, we suggest that the layer-parallel shortening and shearing were in response to outward translation of individual sheets, with a large degree of frictional coupling between the overlying layers. In contrast, the extensional strains are probably in response to an overall vertical thickening of the intrusion, and are found in layers that are not in direct contact with the magma sheets. The bedding-parallel faults observed at the sedimentary contacts must decouple these zones from one another.

6.5. Emplacement model

We envision an incremental emplacement model for the TMI in which vertical and horizontal increments of growth occur through intrusion of multiple magma sheets (Figs. 14 and 16). The accumulation of sheets results in a flat-topped intrusion, which is the most common shape for the top of a laccolith (Corry, 1988). At the WNW outcrop, all the sheets stopped their lateral migration at generally the same outward distance resulting in a steep lateral margin. These observations are similar to the observations at the Maiden Creek sill that is composed of at least two sheets (Horsman et al., 2005).

We interpret the tongue-like sheets on top of the TMI (sheet A in Fig. 4) in the WNW outcrop to have been some of the initial intrusions, emplaced prior to the stacking of the sheets beneath, simply because they are rotated and extend down further along the contact than any of the underlying sheets. The other possibility is that they intruded after the main phase of growth, but along the margin that was already domed. A possible analog to the first case was documented by Jackson and Pollard (1988), who used paleomagnetic analysis to demonstrate that early sub-horizontal sills now exposed on the southern margin of Mount Hillers were rotated to nearly vertical dips by subsequent inflation of the underlying main intrusive body.

The stacking of sheets caused vertical uplift and forced the mechanically strong massive red sandstone at the margin to bend upward as in a monocline. The thinner bedded and mechanically weaker sandstones and shales at the immediate contact are intensely deformed and dip at a much higher angle than the overlying massive red sandstone (90° vs. 30° respectively, see Fig. 4). We suggest that these thinner beds were intensely deformed by the emplacement of individual sheets. As the sheets advanced with steep frontal terminations, the wall rocks in front rotated up and over the top. The hinge (on the top edge of the steep front of the sheet) propagated through the sandstone layer and away from the middle of the intrusion,
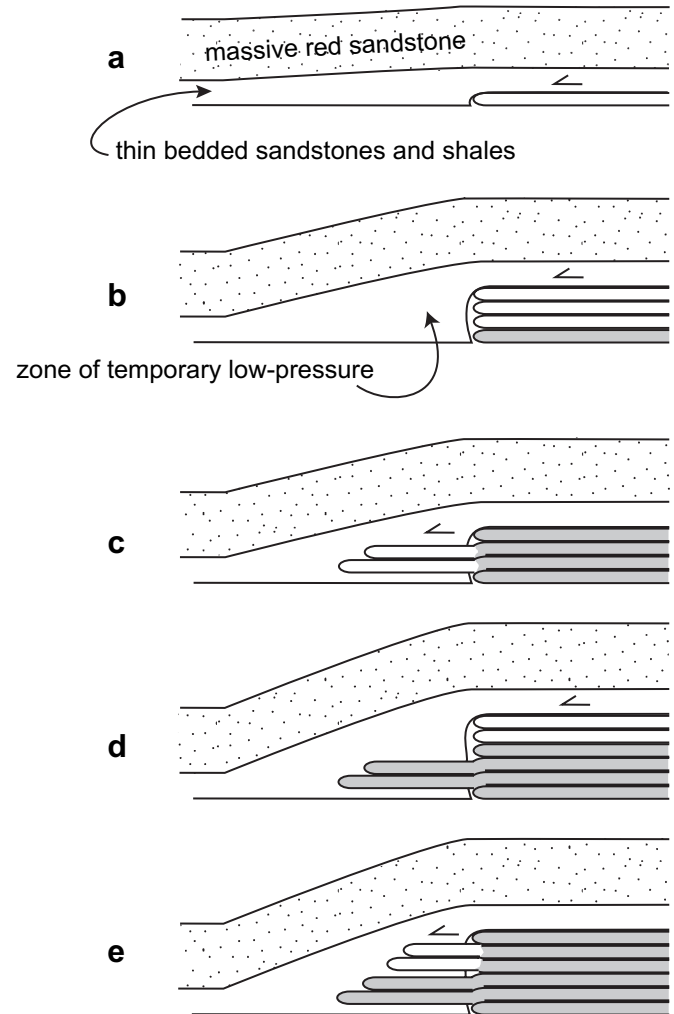
Fig. 16. Emplacement model for the TMI at the WNW outcrop. Not to scale. (a) Single sheet is emplaced and deforms the thin-bedded sedimentary section immediately above. Massive red sandstone (stippled) is slightly uplifted. (b) New sheets (clear) are emplaced on top of older (shaded). Deformation of overlying thin sedimentary rocks rotates bedding to vertical. Massive red sandstone continues to be uplifted. Triangle-shaped zone of low pressure temporarily forms between the front of the laccolith and the uplifted red sandstone. (c) New sheets (clear) emanate from the margin of the laccolith and fill the low-pressure zone. (d) New sheets are emplaced (clear) and continued uplift of the massive red sandstone. (e) New sheets emanate (clear) from the margin of the laccolith to fill the low-pressure zone.

with the front of the advancing sheet, over time. The brecciated wall rocks observed at the front and tops of these sheets support an outward propagating hinge model, as well as the strained sandstone samples from atop the intrusion, more than 100 m from the current margin.

As the intrusion continued to grow vertically by the accumulation of sheets, the angle between the massive red sandstone and the thinner bedded sedimentary layers continued to increase and resulted in a low-pressure triangle-shaped zone in front of the base of the marginal contact (Fig. 16). The low-pressure zone was created because the more massive sandstone layer resisted bending and therefore did not conform exactly to the subvertical outward margin of the growing/stacking laccolith. The thinner bedded sandstones and shales

immediately at the contact were more readily deformed and conformed to the outermost shape of the contact. Because the magma pressure was greater than the lithostatic load (as indicated by the horizontally emplaced magma sheets), the low-pressure region was immediately filled by tongue-like sheets originating from the exterior margin of the accumulating stack. In our model, these tongue-like sheets were emplaced solely as a result of this temporary low-pressure zone. This implies that changes in magma pressure are communicated throughout the growing intrusion, even though the body as a whole is constructed of individual sheets. This model is consistent with the observation that the lower, tongue-like sheets intruded through steeply dipping wall rocks which indicates that these wall rocks had already been rotated to their inclined position before the tongue-like sheets passed through them.

6.6. Previous models

Pollard and Johnson (1973), Koch et al. (1981), Jackson and Pollard (1988), Kerr and Pollard (1998), and Pollard and Fletcher (2005) favor an emplacement model for laccoliths where the elastic properties of the overlying sandstones dictate the shape of laccoliths and they use the TMI as an example. The bending of the overlying rocks is modeled using the equations governing the elastic bending of a thin beam. We suggest that the beam bending model for laccolith growth probably does not apply to the TMI for a variety of reasons. (1) The beam bending model incorrectly assumes that a laccolith will begin to inflate from a sill when the sill has grown horizontally enough so that the magma has enough leverage on the overlying sandstone layers to begin to bend them upward. Our data indicate that the TMI is made of numerous sheets, which are emplaced at different times, and which originated in the center and moved outward. The presence of sheets does not conform to the single magma chamber model where magma pressure is concentrated in the middle. (2) The beam bending model does not predict the observed geometry. The elastic beam model assumes that the massive red sandstone behaves as a single beam and its elastic properties dictate the shape of the laccolith and result in a dome-like shape. In fact, the TMI has a flat roof as do most other laccoliths (Corry, 1988). The ''bent'' portion of the massive red sandstone is strictly confined to the margin of the TMI, which is very small compared to the length across the top. (3) Our study indicates the most of the strain is concentrated in a very small volume of rock at the margins and is a result of the outward motion of sheets. Strain is not evenly distributed across the top as might be expected if the strain was due to fluid (magma) pressure pushing upward. (4) The beam-bending model of Kerr and Pollard (1998) also requires vertical subsidence just in front of the pinning point (area just in front of where the ''beam'' begins to deflect upward). If this model were applicable to the TMI, we would observe a downward deflection of stratigraphy immediately away from the lateral margin of the intrusion (i.e. meters or tens of meters northwest of the cross section outcrop). This prediction is not consistent with the observed stratigraphy or with the lack of deformation demonstrated by strain analysis.

6.7. Relationship to intrusions in general

We suggest that the TMI represents the initial stages of upper crustal magma emplacement typical of intrusions. The Maiden Creek sill, located 3 km to the south, is a smaller sheet-like intrusion defined by two sheets stacked upon one another with a similar shear-zone contact between the sheets (Horsman et al., 2005). The Black Mesa intrusion, located 5 km to the SW, is a much thicker intrusion (200 m thick and 1 km diameter) and only displays cryptic evidence for sheeting and incremental assembly (Habert and de Saint Blanquat, 2004; Morgan et al., 2005; de Saint Blanquat et al., 2006). The top of the Black Mesa intrusion exhibits a high strain zone similar to the top of the TMI, but extensive vertical faces around the margin only reveal horizontal zones of anastomosing cataclastic bands that are 1–2 m thick. These zones are separated by 10–20 m of undeformed igneous rock. Shear zones similar to those at the TMI are not observed. The cataclastic zones at the Black Mesa intrusion are similar to the faults and cataclastic fault zones emanating from some of the sheets in the TMI. The field relationships at the TMI indicate that the sheets that are surrounded by cataclastic fault zones intruded late, and therefore it is possible that the cataclastic zones at the Black Mesa intrusion also represent late-forming sheet contacts. The reason the shear zones did not develop between sheets at the Black Mesa intrusion, although the cataclastic bands did, may be a result of the trade-off between temperature and strain rate. The greater thickness of the Black Mesa intrusion resulted in slower cooling, and therefore sheet margins were hotter and shear zones may not have formed during emplacement. The sheets may still have intruded at very high strain rates. The rapid creation of volume by the forceful emplacement of these fast-moving sheets may have resulted in fracture systems (cataclastic zones) emanating from the boundaries of these sheets. Therefore, intrusions that are emplaced into deeper/hotter levels of the crust may not exhibit any evidence for sheeting simply because the higher temperatures do not allow for shear zone development or brittle failure of the surrounding intrusion, regardless of the rate of emplacement.

7. Conclusions

The Trachyte Mesa intrusion was emplaced into the upper crust as a series of sub-horizontally stacked magma sheets. Contacts between sheets are observed at the intrusion margins and are defined by thin shear zones. Shear zones are defined by plagioclase phenocrysts that have undergone severe cataclasis. Sheets vary in their shape but most are meters thick and have steep frontal terminations. Geomorphic and structural data also support the presence of sheets across the top of the TMI.

AMS fabric data from over 100 locations atop the intrusion suggest that the top sheets were fed from a narrow channel that allowed magma to travel from the SW to the NE and then spread laterally. Near their lateral terminations, sheets have a vertical foliation that rotates abruptly at the top contact to become subhorizontal and subparallel to the contact. We

interpret these fabric patterns as indicating plug-flow where the strain is concentrated in thin zones at the contact and probably led to the cataclasis of the plagioclase phenocrysts. The inclined fabric on the top of the TMI is used as a magma flow sense indicator which is supported by the physical model of Kratinová et al. (2006). Deformation of the sedimentary wall rocks is consistent with the sedimentary layering immediately in front of an advancing sheet being translated upward and over the top of the sheet as in an outward-propagating hinge. Sedimentary layers above the immediate contact were deformed by layer-parallel shortening as result of coupling with the underlying sheets as they moved outward. Strain analyses on a thicker sandstone bed above these layers indicates it was deformed by layer parallel extension and was thinned by $\sim$20%. Thinning was accommodated by fracture-induced porosity collapse. Extension occurred as the layer was stretched over the margin of the rising intrusion. Our observations provide evidence of sheeted emplacement of a small upper crustal intrusion. Although evidence of sheeting is clear in this case, similar processes may be absent or obscured in larger, hotter intrusions.

Acknowledgements

Appendix A

AMS parameters from the 73 sites in the gorge (with the letter "g" as a prefix) and from 103 sites on top of the intrusion

Location	K_m	K_1	K_2	K_3	P%	L	F	T
g2	7.10E-03	7.20E-03	7.11E-03	7.00E-03	2.838	1.013	1.016	0.08
g3	7.02E-03	7.08E-03	7.03E-03	6.94E-03	2.064	1.008	1.013	0.20
g4	8.28E-03	8.39E-03	8.29E-03	8.14E-03	2.958	1.012	1.018	0.18
g5	9.02E-03	9.19E-03	9.02E-03	8.84E-03	4.003	1.019	1.021	0.08
g6	9.36E-03	9.47E-03	9.37E-03	9.24E-03	2.475	1.011	1.014	0.18
g7	6.94E-03	7.03E-03	6.93E-03	6.84E-03	2.806	1.014	1.013	−0.03
g8	7.73E-03	7.81E-03	7.75E-03	7.64E-03	2.301	1.009	1.015	0.30
g9	6.44E-03	6.50E-03	6.45E-03	6.37E-03	1.970	1.008	1.013	0.25
g10	8.31E-03	8.40E-03	8.31E-03	8.22E-03	2.157	1.010	1.012	0.05
g11	7.39E-03	7.46E-03	7.39E-03	7.31E-03	2.082	1.009	1.012	0.16
g12	8.15E-03	8.25E-03	8.15E-03	8.05E-03	2.483	1.012	1.013	0.04
g13	8.94E-03	9.03E-03	8.95E-03	8.83E-03	2.268	1.010	1.014	0.18
g14	8.65E-03	8.75E-03	8.67E-03	8.52E-03	2.771	1.010	1.017	0.26
g15	7.55E-03	7.65E-03	7.60E-03	7.41E-03	3.182	1.007	1.025	0.58
g16	9.26E-03	9.45E-03	9.26E-03	9.07E-03	4.217	1.020	1.022	0.04
g17	9.49E-03	9.62E-03	9.52E-03	9.34E-03	2.992	1.010	1.020	0.31
g18	9.31E-03	9.45E-03	9.31E-03	9.15E-03	3.246	1.016	1.017	0.05
g19	8.35E-03	8.46E-03	8.41E-03	8.19E-03	3.281	1.006	1.026	0.60
g20	8.92E-03	9.06E-03	8.96E-03	8.76E-03	3.411	1.011	1.023	0.34
g21	7.92E-03	8.02E-03	7.93E-03	7.80E-03	2.917	1.012	1.017	0.18
g22	7.75E-03	7.85E-03	7.76E-03	7.65E-03	2.711	1.012	1.015	0.08
g23	5.76E-03	5.81E-03	5.76E-03	5.70E-03	1.946	1.009	1.011	0.13
g24	6.26E-03	6.33E-03	6.27E-03	6.18E-03	2.398	1.010	1.014	0.18
g25	7.69E-03	7.77E-03	7.71E-03	7.61E-03	2.119	1.007	1.014	0.29
g26	8.98E-03	9.09E-03	9.00E-03	8.86E-03	2.564	1.009	1.017	0.28
g27	6.62E-03	6.69E-03	6.64E-03	6.53E-03	2.435	1.007	1.017	0.38
g28	9.61E-03	9.74E-03	9.63E-03	9.46E-03	2.916	1.013	1.017	0.16
g29	9.94E-03	1.01E-02	9.96E-03	9.77E-03	3.337	1.014	1.019	0.17
g30	9.35E-03	9.50E-03	9.36E-03	9.18E-03	3.498	1.014	1.021	0.17
g31	8.29E-03	8.39E-03	8.32E-03	8.15E-03	2.925	1.009	1.020	0.41
g32	1.00E-02	1.02E-02	1.00E-02	9.83E-03	3.613	1.015	1.020	0.14
g33	9.93E-03	1.01E-02	9.97E-03	9.72E-03	4.044	1.014	1.026	0.29
g34	9.56E-03	9.70E-03	9.57E-03	9.40E-03	3.169	1.013	1.018	0.15
g35	1.07E-02	1.08E-02	1.07E-02	1.05E-02	3.424	1.017	1.017	0.03
g36	8.93E-03	9.07E-03	8.97E-03	8.77E-03	3.389	1.012	1.023	0.31
g37	9.07E-03	9.14E-03	9.09E-03	8.97E-03	1.919	1.007	1.013	0.38
g38	9.40E-03	9.50E-03	9.43E-03	9.27E-03	2.446	1.008	1.017	0.36
g39	9.42E-03	9.54E-03	9.44E-03	9.29E-03	2.589	1.011	1.015	0.18
g40	8.08E-03	8.20E-03	8.09E-03	7.95E-03	3.164	1.013	1.018	0.14

Appendix (*continued*)

Location	K_m	K_1	K_2	K_3	P%	L	F	T
g41	9.47E-03	9.62E-03	9.49E-03	9.30E-03	3.448	1.014	1.021	0.22
g42	7.72E-03	7.83E-03	7.73E-03	7.58E-03	3.358	1.013	1.020	0.22
g43	7.62E-03	7.75E-03	7.64E-03	7.49E-03	3.447	1.014	1.020	0.18
g44	9.30E-03	9.40E-03	9.30E-03	9.18E-03	2.362	1.011	1.013	0.10
g45	7.25E-03	7.33E-03	7.26E-03	7.17E-03	2.152	1.010	1.012	0.06
g46	8.55E-03	8.64E-03	8.56E-03	8.46E-03	2.186	1.010	1.011	0.06
g47	7.96E-03	8.04E-03	7.97E-03	7.87E-03	2.087	1.008	1.014	0.29
g48	8.24E-03	8.37E-03	8.24E-03	8.11E-03	3.175	1.016	1.015	−0.05
g49	8.74E-03	8.85E-03	8.76E-03	8.62E-03	2.621	1.011	1.015	0.18
g50	7.83E-03	7.93E-03	7.84E-03	7.72E-03	2.702	1.011	1.016	0.15
g51	8.45E-03	8.53E-03	8.46E-03	8.35E-03	2.238	1.009	1.014	0.26
g52	7.85E-03	7.93E-03	7.86E-03	7.77E-03	2.092	1.009	1.012	0.17
g53	7.37E-03	7.45E-03	7.38E-03	7.28E-03	2.311	1.009	1.014	0.27
g54	9.12E-03	9.22E-03	9.13E-03	9.01E-03	2.336	1.010	1.014	0.15
g55	7.47E-03	7.57E-03	7.49E-03	7.35E-03	2.919	1.010	1.019	0.30
g56	8.91E-03	9.01E-03	8.94E-03	8.78E-03	2.618	1.007	1.019	0.46
g57	7.51E-03	7.60E-03	7.53E-03	7.40E-03	2.699	1.009	1.018	0.34
g58	8.63E-03	8.72E-03	8.65E-03	8.51E-03	2.526	1.009	1.016	0.26
g59	9.44E-03	9.55E-03	9.45E-03	9.32E-03	2.522	1.011	1.014	0.13
g60	9.60E-03	9.72E-03	9.60E-03	9.48E-03	2.514	1.013	1.013	0.00
g61	3.60E-04	3.66E-04	3.59E-04	3.54E-04	3.523	1.020	1.016	0.17
g62	9.81E-03	9.95E-03	9.83E-03	9.66E-03	2.954	1.011	1.018	0.23
g63	7.09E-03	7.16E-03	7.11E-03	7.01E-03	2.185	1.007	1.014	0.34
g64	7.24E-03	7.29E-03	7.23E-03	7.20E-03	1.236	1.009	1.004	−0.36
g65	8.51E-03	8.58E-03	8.51E-03	8.44E-03	1.703	1.009	1.009	0.02
g66	8.97E-03	9.09E-03	8.95E-03	8.86E-03	2.660	1.016	1.011	−0.20
g67	6.97E-03	7.05E-03	6.98E-03	6.87E-03	2.730	1.011	1.017	0.23
g68	7.47E-03	7.55E-03	7.48E-03	7.39E-03	2.067	1.010	1.011	0.09
g69	7.57E-03	7.64E-03	7.56E-03	7.51E-03	1.651	1.010	1.007	−0.18
g70	3.91E-03	3.94E-03	3.92E-03	3.86E-03	2.062	1.007	1.014	0.38
g71	6.84E-03	6.91E-03	6.86E-03	6.73E-03	2.555	1.007	1.019	0.51
g72	9.47E-03	9.60E-03	9.48E-03	9.34E-03	2.757	1.012	1.015	0.12
g73	7.15E-03	7.22E-03	7.18E-03	7.05E-03	2.362	1.006	1.018	0.52
g74	1.85E-03	1.86E-03	1.86E-03	1.83E-03	1.776	1.004	1.014	0.58
1	1.06E-02	1.07E-02	1.06E-02	1.04E-02	3.074	1.014	1.016	0.06
2	8.61E-03	8.69E-03	8.64E-03	8.50E-03	2.198	1.006	1.016	0.44
3	9.95E-03	1.01E-02	9.98E-03	9.83E-03	2.265	1.008	1.015	0.33
4	9.48E-03	9.57E-03	9.49E-03	9.37E-03	2.126	1.008	1.013	0.20
5	1.07E-02	1.09E-02	1.07E-02	1.06E-02	2.649	1.012	1.015	0.11
6	9.68E-03	9.79E-03	9.69E-03	9.56E-03	2.419	1.010	1.014	0.14
7	1.02E-02	1.04E-02	1.02E-02	1.01E-02	3.143	1.012	1.020	0.26
8	1.13E-02	1.14E-02	1.13E-02	1.11E-02	2.723	1.013	1.014	0.02
9	1.20E-02	1.21E-02	1.20E-02	1.18E-02	2.542	1.011	1.014	0.10
10	1.21E-02	1.23E-02	1.21E-02	1.19E-02	2.820	1.012	1.016	0.16
11	1.19E-02	1.20E-02	1.19E-02	1.17E-02	2.604	1.010	1.015	0.19
12	7.78E-03	7.87E-03	7.78E-03	7.68E-03	2.567	1.012	1.014	0.09
13	9.43E-03	9.56E-03	9.43E-03	9.31E-03	2.705	1.014	1.013	−0.04
14	1.03E-02	1.04E-02	1.03E-02	1.01E-02	2.656	1.010	1.016	0.21
15	1.08E-02	1.09E-02	1.07E-02	1.06E-02	3.023	1.017	1.013	−0.13
16	1.04E-02	1.06E-02	1.05E-02	1.02E-02	3.255	1.008	1.025	0.51
17	1.09E-02	1.11E-02	1.09E-02	1.07E-02	3.064	1.014	1.017	0.09
18	1.19E-02	1.21E-02	1.19E-02	1.18E-02	2.622	1.012	1.014	0.06
19	1.17E-02	1.20E-02	1.17E-02	1.15E-02	3.659	1.022	1.014	−0.23
20	1.14E-02	1.15E-02	1.14E-02	1.12E-02	2.611	1.009	1.017	0.33
21	1.07E-02	1.09E-02	1.08E-02	1.06E-02	3.038	1.008	1.022	0.45
22	1.03E-02	1.04E-02	1.03E-02	1.01E-02	2.711	1.007	1.020	0.51
23	9.07E-03	9.17E-03	9.11E-03	8.92E-03	2.787	1.007	1.020	0.47
24	1.11E-02	1.13E-02	1.11E-02	1.10E-02	3.123	1.016	1.015	−0.03
25	1.00E-02	1.02E-02	1.01E-02	9.89E-03	3.025	1.013	1.017	0.15
26	8.31E-03	8.43E-03	8.35E-03	8.17E-03	3.192	1.009	1.022	0.41
27	8.78E-03	8.89E-03	8.82E-03	8.61E-03	3.237	1.008	1.024	0.51
28	9.24E-03	9.39E-03	9.23E-03	9.10E-03	3.201	1.017	1.014	−0.09
29	9.32E-03	9.49E-03	9.33E-03	9.15E-03	3.711	1.017	1.020	0.08
30	9.51E-03	9.63E-03	9.52E-03	9.36E-03	2.872	1.012	1.017	0.18

Appendix (continued)

Location	K_m	K_1	K_2	K_3	P%	L	F	T
31	1.00E-02	1.02E-02	1.01E-02	9.87E-03	2.910	1.010	1.019	0.30
32	1.19E-02	1.21E-02	1.19E-02	1.17E-02	3.071	1.014	1.016	0.08
33	9.28E-03	9.40E-03	9.28E-03	9.16E-03	2.635	1.012	1.014	0.09
34	8.53E-03	8.62E-03	8.56E-03	8.40E-03	2.617	1.008	1.018	0.41
35	1.21E-02	1.23E-02	1.21E-02	1.19E-02	2.600	1.013	1.013	0.03
36	8.41E-03	8.52E-03	8.41E-03	8.30E-03	2.605	1.013	1.012	−0.02
37	5.06E-03	5.14E-03	5.07E-03	4.97E-03	2.752	1.013	1.014	0.01
38	1.14E-02	1.16E-02	1.14E-02	1.12E-02	3.461	1.015	1.019	0.12
39	1.04E-02	1.06E-02	1.05E-02	1.03E-02	2.811	1.011	1.017	0.24
40	7.92E-03	8.04E-03	7.92E-03	7.80E-03	3.043	1.015	1.015	0.03
41	7.13E-03	7.22E-03	7.13E-03	7.05E-03	2.413	1.013	1.011	−0.08
42	9.85E-03	9.98E-03	9.87E-03	9.71E-03	2.829	1.011	1.017	0.20
43	6.28E-03	6.34E-03	6.30E-03	6.20E-03	2.242	1.007	1.015	0.31
44	9.33E-03	9.47E-03	9.36E-03	9.16E-03	3.328	1.012	1.021	0.29
45	6.58E-03	6.65E-03	6.59E-03	6.50E-03	2.143	1.010	1.011	0.03
46	7.17E-03	7.27E-03	7.19E-03	7.06E-03	2.901	1.011	1.018	0.26
47	9.67E-03	9.76E-03	9.69E-03	9.56E-03	2.083	1.007	1.014	0.33
48	6.11E-03	6.18E-03	6.11E-03	6.03E-03	2.422	1.011	1.013	0.10
49	9.37E-03	9.50E-03	9.40E-03	9.22E-03	3.013	1.011	1.019	0.29
50	6.26E-03	6.34E-03	6.27E-03	6.16E-03	2.987	1.012	1.018	0.24
52	6.50E-03	6.59E-03	6.52E-03	6.41E-03	2.767	1.010	1.018	0.33
53	8.50E-03	8.60E-03	8.50E-03	8.39E-03	2.551	1.012	1.014	0.07
54	7.10E-03	7.19E-03	7.10E-03	7.00E-03	2.698	1.012	1.015	0.09
55	8.28E-03	8.38E-03	8.30E-03	8.16E-03	2.657	1.010	1.016	0.24
56	7.44E-03	7.53E-03	7.44E-03	7.34E-03	2.617	1.012	1.014	0.03
57	1.05E-02	1.07E-02	1.05E-02	1.03E-02	3.238	1.013	1.020	0.22
58	8.63E-03	8.74E-03	8.65E-03	8.51E-03	2.666	1.010	1.017	0.26
59	9.96E-03	1.01E-02	9.98E-03	9.81E-03	2.826	1.011	1.017	0.19
60	6.26E-03	6.34E-03	6.25E-03	6.20E-03	2.285	1.014	1.009	−0.18
61	4.58E-03	4.63E-03	4.59E-03	4.52E-03	2.371	1.008	1.015	0.30
62	9.51E-03	9.60E-03	9.55E-03	9.36E-03	2.631	1.005	1.021	0.59
63	4.91E-03	4.95E-03	4.93E-03	4.86E-03	1.958	1.005	1.015	0.56
64	6.03E-03	6.10E-03	6.03E-03	5.95E-03	2.412	1.011	1.014	0.14
65	7.20E-03	7.28E-03	7.20E-03	7.11E-03	2.327	1.010	1.013	0.14
66	5.92E-03	5.98E-03	5.92E-03	5.85E-03	2.241	1.010	1.012	0.19
67	7.92E-03	8.02E-03	7.94E-03	7.81E-03	2.698	1.010	1.017	0.29
68	4.50E-03	4.54E-03	4.53E-03	4.43E-03	2.587	1.003	1.023	0.80
69	6.12E-03	6.19E-03	6.15E-03	6.03E-03	2.739	1.007	1.020	0.48
70	4.40E-03	4.44E-03	4.42E-03	4.34E-03	2.456	1.005	1.020	0.63
71	6.87E-03	6.94E-03	6.90E-03	6.76E-03	2.540	1.005	1.020	0.64
72	7.70E-03	7.81E-03	7.69E-03	7.60E-03	2.727	1.016	1.012	−0.14
73	1.07E-02	1.09E-02	1.08E-02	1.05E-02	3.161	1.009	1.022	0.40
74	5.89E-03	5.95E-03	5.91E-03	5.82E-03	2.260	1.006	1.017	0.49
75	6.50E-03	6.58E-03	6.50E-03	6.41E-03	2.599	1.012	1.014	0.05
76	7.64E-03	7.72E-03	7.67E-03	7.53E-03	2.500	1.006	1.019	0.55
77	8.48E-03	8.59E-03	8.51E-03	8.33E-03	3.077	1.009	1.021	0.39
78	6.95E-03	7.05E-03	6.98E-03	6.81E-03	3.447	1.011	1.024	0.38
79	7.21E-03	7.33E-03	7.23E-03	7.08E-03	3.519	1.015	1.020	0.14
80	4.20E-03	4.28E-03	4.21E-03	4.11E-03	4.209	1.017	1.025	0.19
81	9.73E-03	9.97E-03	9.71E-03	9.50E-03	4.877	1.026	1.022	−0.09
82	7.03E-03	7.18E-03	7.00E-03	6.91E-03	3.939	1.026	1.014	−0.29
83	7.13E-03	7.24E-03	7.13E-03	7.00E-03	3.427	1.016	1.018	0.06
84	2.33E-04	2.38E-04	2.32E-04	2.28E-04	3.841	1.020	1.018	−0.02
85	9.16E-03	9.26E-03	9.18E-03	9.03E-03	2.585	1.009	1.016	0.28
86	7.39E-03	7.49E-03	7.41E-03	7.26E-03	3.037	1.010	1.020	0.31
87	8.61E-03	8.73E-03	8.61E-03	8.49E-03	2.810	1.014	1.014	0.01
88	8.19E-03	8.28E-03	8.20E-03	8.09E-03	2.333	1.009	1.014	0.17
89	7.48E-03	7.55E-03	7.50E-03	7.40E-03	1.993	1.006	1.013	0.33
90	7.39E-03	7.46E-03	7.42E-03	7.29E-03	2.329	1.005	1.018	0.54
91	6.64E-03	6.72E-03	6.64E-03	6.55E-03	2.542	1.012	1.013	0.04
92	1.01E-02	1.03E-02	1.02E-02	9.98E-03	3.239	1.015	1.017	0.04
93	1.04E-02	1.05E-02	1.04E-02	1.03E-02	2.781	1.013	1.015	0.08
94	4.60E-03	4.67E-03	4.61E-03	4.53E-03	2.891	1.013	1.016	0.09
95	7.64E-03	7.74E-03	7.68E-03	7.50E-03	3.067	1.008	1.023	0.47

Appendix (*continued*)

Location	K_m	K_1	K_2	K_3	P%	L	F	T
96	6.55E-03	6.62E-03	6.56E-03	6.46E-03	2.608	1.010	1.016	0.23
97	1.10E-02	1.11E-02	1.10E-02	1.08E-02	2.810	1.014	1.014	0.02
98	1.16E-02	1.17E-02	1.15E-02	1.14E-02	2.800	1.014	1.014	−0.02
99	6.88E-03	6.95E-03	6.89E-03	6.79E-03	2.252	1.008	1.014	0.25
100	7.34E-03	7.42E-03	7.35E-03	7.24E-03	2.560	1.010	1.015	0.21
101	6.70E-03	6.79E-03	6.70E-03	6.59E-03	3.058	1.013	1.017	0.11
102	7.68E-03	7.76E-03	7.69E-03	7.60E-03	2.167	1.010	1.012	0.11
103	7.85E-03	7.93E-03	7.85E-03	7.75E-03	2.350	1.011	1.013	0.11
Averages	8.31E-03	8.41E-03	8.32E-03	8.19E-03	2.749	1.011	1.016	0.20
Maximum	1.21E-02							
Minimum	2.33E-04							

References

Arbaret, L., Diot, H., Bouchez, J.L., Lespinasse, P., de Saint Blanquat, M., 1997. Analogue 3D simple shear experiments of magmatic biotite subfabrics. In: Bouchez, J.L., Hutton, D.H.W., Stephens, W.E. (Eds.), Granite: From Segregation of Melt to Emplacement Fabrics. Kluwer Academic Publishers, Dordrecht, pp. 129−143.

Bouchez, J.L., 1997. Granite is never isotropic: an introduction to AMS studies of granitic rocks. In: Bouchez, J.L., Hutton, D.H.W., Stephens, W.E. (Eds.), Granite: From Segregation of Melt to Emplacement Fabrics. Kluwer Academic Publishers, Dordrecht, pp. 95−112.

Cigolini, C., Borgia, A., Casertano, L., 1984. Intra-crater activity, AA-block lava, viscosity and flow dynamics: Arenal volcano, Costa Rica. Journal of Volcanology and Geothermal Research 20, 155−176.

Clemens, J.D., Mawer, C.K., 1992. Granitic magma transport by fracture propagation. Tectonophysics 204, 339−360.

Coleman, D.S., Gray, W., Glazner, A.F., 2004. Rethinking the emplacement and evolution of zoned plutons; geochronologic evidence for incremental assembly of the Tuolumne Intrusive Suite, California. Geology 32, 433−436.

Corry, C.E., 1988. Laccoliths; Mechanics of emplacement and growth. Geological Society of America Special Paper No. 220.

Davis, G., 1999. Structural geology of the Colorado Plateau region of southern Utah, with special emphasis on deformation bands. Geological Society of America Special Paper No. 342.

de Saint Blanquat, M., Habert, G., Horsman, E., Morgan, S.S., Tikoff, B., Launeau, P., Gleizes, G., 2006. Mechanisms and duration of non-tectonically assisted magma emplacement in the upper crust: the Black Mesa pluton, Henry Mountains, Utah. Tectonophysics 428, 1−31.

Engel, C.G., 1959. Igneous rocks and constituent hornblendes of the Henry Mountains, Utah. Geological Society of America Bulletin 70, 951−980.

Erslev, E., 1988. Normalized center-to-center strain analysis of packed aggregates. Journal of structural Geology 10, 201−209.

Fry, N., 1979. Random point distributions and strain measurements in rocks. Tectonophysics 60, 89−105.

Gaillot, P., de Saint Blanquat, M., Bouchez, J.-L., 2006. Effects of magnetic interactions in anisotropy of magnetic susceptibility: discussion on models and experiments—implications for the quantification of rock fabrics. Tectonophysics 418, 3−19.

Gilbert, G.K., 1877, Report on the Geology of the Henry Mountains. U.S. Geographical and Geological Survey, Rocky Mountains Region.

Glazner, A.F., Bartley, J.M., Coleman, D.S., Gray, W., Taylor, R.Z., 2004. Are plutons assembled over millions of years by amalgamation from small magma chambers? GSA Today 14, 4−11.

Gonnermann, H., Manga, M., 2003. Explosive volcanism may not be an inevitable consequence of magma fragmentation. Nature 426, 432−435.

Grégoire, V., de Saint Blanquat, M., Nedelec, A., Bouchez, J.-L., 1995. Shape anisotropy versus magnetic interactions of magnetite grains; experiments and application to AMS in granitic rocks. Geophysical Research Letters 22, 2765−2768.

Habert, G., de Saint Blanquat, M., 2004. Rate of construction of the Black Mesa bysmalith, Henry Mountains, Utah. In: Beitkreuz, C., Petford, N. (Eds.), Physical Geology of High-Level Magmatic Systems. Geological Society Special Publication, vol. 234. Geological Society, London, pp. 163−173.

Hansen, D.M., Cartwright, J., 2006. Saucer-shaped sills with lobate morphology revealed by 3-d seismic data: implications for resolving a shallow-level sill emplacement mechanism. Journal of the Geological Society 163, 509−523.

Harper, B.E., Miller, C.F., Koteas, G.C., Cates, N.L., Wiebe, R.A., Lazzareschi, D.S., Cribb, J.W., 2004. Granites, dynamic magma chamber processes and pluton construction: the Aztec Wash pluton, Eldorado Mountains, Nevada, USA. Transactions of the Royal Society of Edinburgh: Earth Sciences 95, 277−295.

Harris, A.J.L., Flynn, L.P., Matías, O., Rose, W.I., 2002. The thermal stealth flows of Santiaguito dome, Guatemala: Implications for the cooling and emplacement of dacitic block-lava flows. Geological Society of America Bulletin 114, 533−546.

Horsman, E., Tikoff, B., Morgan, S.S., 2005. Emplacement-related fabric in a sill and multiple sheets in the Maiden Creek sill, Henry Mountains, Utah. Journal of Structural Geology 27, 1426−1444.

Hunt, C.B., 1953. Geology and geography of the Henry Mountains region, Utah: U.S. Geological Survey Professional Paper 228, 234 pp.

Jackson, M.D., Pollard, D.D., 1988. The laccolith-stock controversy: New results from the southern Henry Mountains, Utah. Geological Society of America Bulletin 100, 117−139.

Johnson, S.E., Vernon, R.H., 2004. Foliation development and progressive strain-rate partitioning in the crystallizing carapace of a tonalite pluton; microstructural evidence and numerical modeling. Geological Society of America Bulletin 26, 1845−1865.

Kerr, A.D., Pollard, D.D., 1998. Toward more realistic formulations for the analysis of laccoliths. Journal of Structural Geology 20, 1783−1793.

Kilburn, C.R.J., Guest, J.E., 1993. Aa lavas of Mount Etna, Sicily. In: Kilburn, C.R.J., Luongo, G. (Eds.), Active Lavas: Monitoring and Modelling. UCL Press, London, pp. 73−106.

Koch, F.G., Johnson, A.M., Pollard, D.D., 1981. Monoclinal bending of strata over laccolithic intrusions. Tectonophysics 74, T21−T31.

Komar, P.D., 1972. Mechanical interactions of phenocrysts and flow differentiation of igneous dikes and sills. Geological Society of America Bulletin 83, 973−988.

Kratinová, Z., Zavada, P., Hrouda, F., Schulmann, K., 2006. Non-scaled analogue modelling of AMS development during viscous flow: A simulation on diapir-like structures. Tectonophysics 418, 51−61.

Le Bas, M.J., Le Maitre, R.W., Streckeisen, A., Zanettin, B., 1986. A chemical classification of volcanic rocks based on the total alkali-silica diagram. Journal of Petrology 27, 745−750.

Mahan, K.H., Bartley, J.M., Coleman, D.S., Glazner, A.F., Carl, B., 2003. Sheeted intrusion of the synkinematic McDoogle pluton, Sierra Nevada, California. Geological Society of America Bulletin 115, 1570−1582.

Matzel, J.E.P., Bowring, S.A., Miller, R.B., 2006. Time scales of pluton construction at differing crustal levels; examples from the Mount Stuart and Tenpeak Intrusions, north Cascades, Washington. Geological Society of America Bulletin 118, 1412–1430.

McNulty, B.A., Tong, W., Tobisch, O.T., 1996. Assembly of a dike-fed magma chamber: The Jackass Lakes pluton, central Sierra Nevada, California. Geological Society of America Bulletin 108, 926–940.

Morgan, S.S., Horsman, E., Tikoff, B., de Saint Blanquat, M., Nugent, A., Habert, G., 2005. Sheet-like emplacement of satellite laccoliths, sills, and bysmaliths of the Henry Mountains, southern Utah. In: Pederson, J., Dehler, C.M. (Eds.), Interior Western United States Field Guide 6. Geological Society of America, pp. 283–309.

Nelson, S.T., Davidson, J.P., Sullivan, K.R., 1992. New age determinations of central Colorado Plateau laccoliths, Utah: Recognizing disturbed K-Ar systematics and re-evaluating tectonomagmatic relationships. Geological Society of America Bulletin 104, 1547–1560.

Nelson, S.T., Davidson, J.P., 1993. Interactions between mantle-derived magmas and mafic crust, Henry Mountains, Utah. Journal of Geophysical Research 98, 1837–1852.

Petford, N., 1996. Dykes or diapirs? Transactions of the Royal Society of Edinburgh: Earth Sciences 87, 105–114.

Pollard, D.D., Fletcher, 2005. Fundamentals of Structural Geology. Cambridge University Press, New York.

Pollard, D.D., Johnson, A.M., 1973. Mechanics of growth of some laccolith intrusions in the Henry mountains, Utah, II; bending and failure of overburden layers and sill formation. Tectonophysics 18, 311–354.

Pollard, D.D., Muller, O.H., Dockstader, D.R., 1975. The form and growth of fingered sheet intrusions. Geological Society of America Bulletin 86, 351–363.

Rochette, P., Jackson, M., Aubourg, C., 1992. Rock magnetism and the interpretation of anisotropy of magnetic susceptibility. Reviews of Geophysics 30, 209–226.

Ross, M.E., 1986. Flow differentiation, phenocryst alignment, and compositional trends within a dolerite dike at Rockport, Massachusetts. Geological Society of America Bulletin 97, 232–240.

Shipton, Z.K., Cowie, P.A., 2001. Damage zone and slip-surface evolution over μm to km scales in high-porosity Navajo sandstone, Utah. Journal of Structural Geology 23, 1825–1844.

Sullivan, K.R., Kowallis, B.J., Mehnert, H.H., 1991. Isotopic ages of igneous intrusions in southeastern Utah: Evidence for a mid-Cenozoic Reno-San Juan magmatic zone. Brigham Young University Geology Studies 37, 139–144.

Symons, D.T.A., Cioppa, M.T., 2000. Crossover plots: a useful method for plotting SIRM data in paleomagnetism. Geophysical Research Letters 27, 1779–1782.

Tarling, D.H., Hrouda, F., 1993. The Magnetic Anisotropy of Rocks. Chapman & Hall, New York, 217 pp.

Thomson, K., Hutton, D., 2004. Geometry and growth of sill complexes: insights using 3-d seismic from the North Rockall Trough. Bulletin of Volcanology 66, 364–375.

Wiebe, R.A., 2003. The Pleasant Bay layered gabbro-diorite, coastal Maine; ponding and crystallization of basaltic injections into a silicic magma chamber. Journal of Petrology 34, 461–489.

Zhang, J., Wong, T.-F., Yanagidani, T., Davis, D.M., 1990. Pressure-induced microcracking and grain crushing in Berea and Baise sandstones: acoustic emission and quantitative microscopy measurements. Mechanics of Materials 9, 1–15.